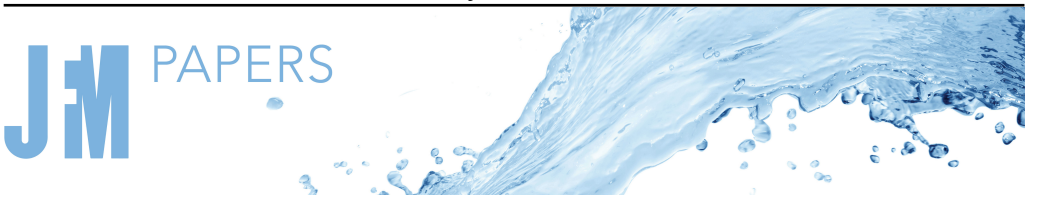
J. Fluid Mech. (2026), *vol.* 1044, A20, doi:10.1017/jfm.2026.12123



Cavitation bubble-induced shear flow and stress within grooved structures

Shi-Min Li[1,2], **A-Man Zhang**[1,2], **Da-Hao Xie**[1,2], **Hongjie An**[3] and **Qingyun Zeng**[1,2]

[1]Sanya Nanhai Innovation and Development Base of Harbin Engineering University, Sanya 572024, PR China

[2]College of Shipbuilding Engineering, Harbin Engineering University, Harbin 150001, PR China

[3]Queensland Micro and Nanotechnology Centre, Griffith University, Nathan, QLD 4111, Australia

Corresponding authors: Qingyun Zeng, qyzeng@hrbeu.edu.cn; A-Man Zhang, zhangaman@hrbeu.edu.cn

(Received 4 March 2026 UTC; revised 17 July 2026 UTC; accepted 15 August 2026 UTC)

The shear flow induced by a jetting cavitation bubble within grooved structures is systematically investigated using a three-dimensional compressible volume-of-fluid (VoF) solver combined with ultra-high-speed photography of one million frames per second (fps). The structured surface comprises twenty parallel micro-channels, and local mesh refinement down to 0.1 μm near the groove bottom resolves the linear tangential velocity profile within the boundary layer. The simulations accurately reproduce experimental observations for two representative configurations, namely bubbles initiated above the groove and above the protrusion. In general, a microjet formed from the distal bubble surface impacts the lower bubble interface and subsequently spreads both along and across the groove channel, generating strong shear flow. Spatio-temporal wall-stress distributions indicate that the maximum shear stress occurs near the instant of jet impact, while the subsequent evolution is further modulated by daughter-bubble fragmentation and re-expansion. For a bubble initiated above the groove, the microjet produces a single impact, whereas for a bubble initiated above the protrusion, the jet becomes oblique: it first strikes the protrusion, spreads into the trapped bubble inside the groove and finally pierces the lower bubble surface at an angle. The influences of three geometric parameters, namely the horizontal offset d^*, vertical stand-off distance h^* and groove width w^*, are systematically examined, revealing their coupled effects on bubble deformation, jet orientation, fragmentation and the vortex dynamics. A peak wall-shear stress of approximately 150 kPa is obtained under specific geometric conditions due to rapid jet spreading and flow refocusing within the groove. These results provide fundamental

https://doi.org/10.1017/jfm.2026.12123 Published online by Cambridge University Press

© The Author(s), 2026. Published by Cambridge University Press.

insight into the three-dimensional, unsteady wall-shear generation produced by jetting cavitation bubbles interacting with micro-structured surfaces.

Key words: cavitation, bubble dynamics

1. Introduction

The collapse of cavitation bubbles, accompanied by high-speed microjets and shock waves, is widely observed in both natural phenomena (Veron *et al.* 2012) and engineering applications, including biological engineering (Rau *et al.* 2006; Ohl *et al.* 2006*a*), advanced manufacturing (Reuter *et al.* 2017; Landel & Wilson 2021) and chemical engineering (Jana & Bhaskarwar 2010; Nagalingam *et al.* 2023), among others. In the vicinity of rigid surfaces, the asymmetric pressure distribution during bubble collapse drives the formation of a microjet that impacts the surface and subsequently spreads along it prior to the final collapse. Depending on the stand-off distance, the jet velocity can range from tens to several thousand metres per second. Such jets may be detrimental, as they pit solid surfaces and lead to cavitation erosion (Philipp & Lauterborn 1998; Reuter *et al.* 2022*a*), or beneficial, as the associated impulsive pressure loading and intense shear flows can be exploited in applications such as targeted drug delivery (Coussios & Roy 2008; Eleanor & Constantin 2019) and surface cleaning (Ohl *et al.* 2006*b*; Verhaagen & Rivas 2016; Chahine *et al.* 2016). To achieve particular functions, various strategies have been explored to modulate jet morphology and velocity, including the use of complex geometries (Zeng *et al.* 2024), bubble–bubble interaction (Fan *et al.* 2024) and application of acoustic (Cattaneo *et al.* 2025) and electric (Taleghani *et al.* 2023) fields.

While the canonical dynamics of bubble collapse near a flat, rigid wall has been systematically investigated in earlier studies (Blake *et al.* 1986; Brujan *et al.* 2002; Zhang *et al.* 2006; Reuter *et al.* 2022*b*), practical scenarios often involve multiple and complex boundary conditions, for which improved models are still required to elucidate the underlying fluid mechanics. For example, in precision cleaning of instruments such as microchips and sensors, the relevant surfaces typically exhibit complex topographies, with micro-scale structural features arranged in arrays (Kim & Kim 2014). Under these conditions, bubbles undergo complex deformations driven by the combined effects of rapid expansion and collapse and the associated transient boundary-layer flows (Zeng *et al.* 2020). As a result, microjet formation becomes strongly modified owing to symmetry breaking induced by the complex geometry (Brujan *et al.* 2022) in shape and velocity.

A further step towards realistic conditions is the consideration of a bubble dynamics confined by combined boundaries, such as that between parallel walls (Kucherenko & Shamko 1986; Hsiao *et al.* 2013; Zeng *et al.* 2020), near crossed walls (Brujan *et al.* 2018; Tagawa & Peters 2018; Wang *et al.* 2020) or in a rectangular corner (Molefe & Peters 2019; Brujan *et al.* 2022), where geometric symmetry breaking has been shown to alter jet direction and the overall collapse scenario. In addition, research attention has been extended to cavitation bubbles interacting with isolated solid objects of various shapes, including spherical particles (Poulain *et al.* 2015; Wu *et al.* 2017) and surface pits (Chao-Tsung *et al.* 2014; Trummler *et al.* 2020). However, these boundary conditions are still largely restricted to fundamental and regular geometries, with characteristic length scales that are much larger than those of the micro-structured features commonly encountered on precision-engineered surfaces.

Research on the cavitation-bubble dynamics near structured surfaces has primarily focused on macroscopic characteristics, such as overall bubble behaviour and jet

https://doi.org/10.1017/jfm.2026.12123 Published online by Cambridge University Press

velocity (Trummler *et al.* 2020; Andrews *et al.* 2020, 2023). In contrast, the wall-shear stress, indicating the flow shear rate within the boundary layer, a quantity crucial for applications including surface cleaning and cell membrane poration (Ohl *et al.* 2006*b*; Kim *et al.* 2009), has been largely overlooked. In recent years, however, direct quantitative analysis of wall-shear stress has attracted increasing attention. Zeng *et al.* (2018) employed a finite-volume method to compute the spatio-temporal distribution of wall-shear stress on a flat wall induced by a collapsing bubble, demonstrating that peak shear stresses generated by jetting bubbles can reach tens of kilopascals and last for a short duration. Subsequent studies have further elucidated the influence of parameters such as liquid viscosity and stand-off distance on the wall-shear stress (Zeng *et al.* 2022). A major challenge in extending such analyses lies in the large disparity between the boundary-layer thickness near the wall and the characteristic bubble size, which leads to prohibitive computational costs. As a result, most quantitative studies of wall-shear stress remain restricted to axisymmetric configurations (Mohammadzadeh *et al.* 2017; Mifsud *et al.* 2021; Reese *et al.* 2023). When complex microstructures are present on precision-engineered surfaces, the interaction between the jet and these features gives rise to fully three-dimensional and unsteady flow fields. Nevertheless, the resulting shear-stress distributions on three-dimensional micro-structured surfaces and their dependence on geometric parameters remain largely unexplored.

We therefore consider a more realistic configuration: a grooved surface composed of an array of rectangular protrusions forming slender channels, as shown in figure 1. The objective is to resolve the shear flow and wall-shear stress generated within the grooves by collapsing cavitation bubbles.

The high-resolution simulations of Zeng *et al.* (2018) showed that the maximum shear rate induced by a jetting bubble near a rigid surface can reach $10^8\ \mathrm{s}^{-1}$, with the tangential velocity increasing from 0 to $100\ \mathrm{m\,s}^{-1}$ within approximately $1\ \mu\mathrm{m}$. This indicates that direct measurement of the wall-shear stress requires resolving the flow within only a few micrometres of the rigid boundary. In addition, the stress peak, which can reach $\mathcal{O}(100)$ kPa, decays significantly within approximately $10\ \mu\mathrm{s}$, requiring a measurement technique with both a high sampling frequency, exceeding 100 kHz, and a sufficiently large bandwidth. Existing measurements using a hot-film anemometer (Dijkink & Ohl 2008) and an electrochemical method (Reuter & Mettin 2018) reported peak wall-shear stresses of the order of a few kilopascals. These approaches provide valuable experimental evidence, but they are intrinsically limited by their finite spatial resolution and temporal response. A comparison between simulations and experimental measurements over the same effective sensor area shows good agreement in the overall temporal shape and main features of the shear-stress signal, although the peak values may differ by one to two orders of magnitude (Zeng *et al.* 2018). An approximate analysis of this discrepancy, based on sensor bandwidth, spatial resolution and intrusiveness, can be found on pp. 44–45 of Zeng (2020).

In the present study, resolving transient shear stresses inside a $200\ \mu\mathrm{m}$-wide groove during a microsecond-scale cavitation event is even more challenging. The difficulty arises from the limited optical access to the groove bottom, the strongly three-dimensional nature of the stress field and the very small thickness of the near-wall linear velocity region, which is typically only a few micrometres or less. Therefore, the experiments are used to validate the bubble morphology and jet timing, while the wall-shear stress is obtained from the validated three-dimensional simulations.

To this end, we develop a three-dimensional volume-of-fluid (VoF) solver for the bubble dynamics and resolve the near-wall boundary-layer flow using local mesh refinement, enabling accurate capture of the high shear rates expected during jet impact. We focus on the spatio-temporal evolution of the wall-shear stress within the grooved channels.

https://doi.org/10.1017/jfm.2026.12123 Published online by Cambridge University Press

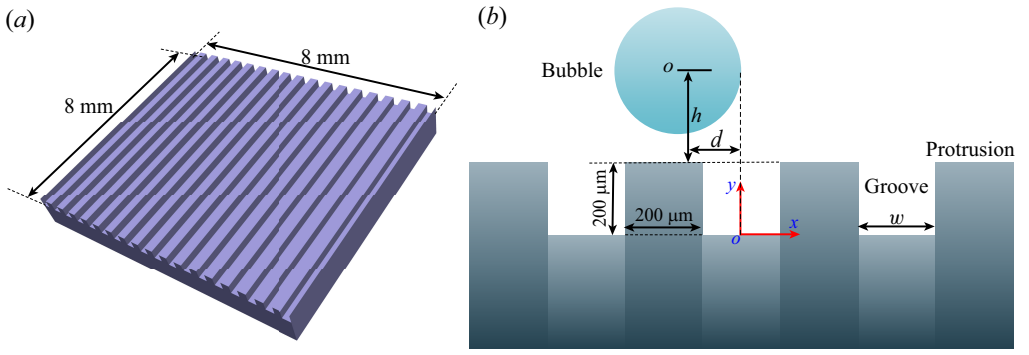


Figure 1. (*a*) Schematic of an 8 mm × 8 mm grooved structure comprising twenty parallel microchannels. (*b*) Coordinates and parameters of the region of interest. The deep-blue features represent a section of the microstructure, with the coordinate origin defined at the centre of the groove base along its central axis. The x- and y-axes are oriented horizontally to the right and vertically upward, respectively. The z axis points out of the plane of the paper. The protrusions between adjacent grooves have fixed dimensions of 0.2 mm × 0.2 mm × 8 mm. The blue circle denotes the nucleation bubble, located at a vertical distance h from the protrusion top and a horizontal distance d from the centre of the nearest groove.

By systematically varying the bubble position and the groove width, the characteristics of the resulting shear flow are elucidated. These results provide new insight into three-dimensional shear-flow generation in grooved microstructures and are relevant to applications involving precision-engineered surfaces.

The remainder of this paper is organised as follows. In § 2, the experimental set-up and numerical methodology are described. In § 3, comparisons of bubble morphology between simulations and experiments are presented for two representative cases. Detailed results are then provided, including bubble deformation, velocity and pressure fields and the spatio-temporal distribution of wall-shear stress at the groove bottom induced by bubble jetting. In § 4, the influence of three key geometric parameters, the horizontal bubble position, the bubble height and the groove width, on the wall-shear flow at the groove bottom is systematically analysed. Finally, the main fluid-mechanical findings are summarised, and perspectives for future work are discussed in § 5.

2. Methodology

2.1. *Physical model*

The physical model and parameter definitions are schematically illustrated in figure 1. Figure 1(*a*) shows the grooved structure with dimensions of 8mm × 8mm, comprising 20 parallel grooves. The inner-groove protrusions and the groove bottom form an array of elongated channels, with the channel width, height and inter-channel spacing fixed at 200 μm. The grooved structure was fabricated via stereolithography 3-D printing using a hydrophilic photopolymer resin. The surface roughness of the printed structure is approximately 10 μm, corresponding to approximately 1 % of the maximum bubble diameter. This roughness is expected to have a negligible influence on the global bubble growth during most of the first oscillation cycle, although it may affect the near-wall-shear flow after jet impact and the very late collapse dynamics. In contrast, the grooved geometry itself strongly influences the local bubble deformation, jet formation and wall-shear stress, as discussed below. The experiments were conducted in a cubic water tank of size 8cm × 8cm × 8cm under the atmospheric pressure $p_\infty = 101\,325$ Pa, with the grooved structure securely mounted on a rigid steel frame. Individual cavitation bubbles are

https://doi.org/10.1017/jfm.2026.12123 Published online by Cambridge University Press

produced by focusing a laser pulse above the grooved structure, producing bubbles with a maximum volume-equivalent radius of approximately 457 μm. The bubble nucleation position was carefully controlled so that all far-field boundaries were located at distances exceeding 50 times the maximum bubble radius R_{max}. The bubble dynamics was recorded from a front view using a high-speed camera (Kirana-7M) operating at 10^6 frames per second with an exposure time of 100 ns. And the illumination is provided by a high-frequency pulsed laser of pulse width 50 ns and frequency of 1 MHz.

Figure 1(*b*) illustrates the coordinate system and parameter definitions. The origin o is defined at the centre of the groove bottom. The x-axis is aligned with the direction of channel width, the y-axis extends vertically upward and the z-axis points out of the plane of the paper. The physical model is symmetric about the plane $z = 0$. Based on this configuration, three characteristic parameters are introduced and discussed in later sections: d, the horizontal distance between the initial bubble and the centre of the groove, h, the vertical distance between the initial bubble and the protrusion top and w, the groove width. The wall-shear stress is therefore evaluated over the domain of $-w/2 < x < w/2$. Bubble dynamics and the resulting flow can be governed by the following three dimensionless parameters:

$$d^* = d/w, \quad h^* = h/R_{max}, \quad w^* = w/R_{max}. \tag{2.1}$$

2.2. *Numerical implementation*

Since the significant heat transfer and phase change occur either within a very narrow region adjacent to the bubble interface or during the short final stage of collapse, their influence on bubble deformation, jet formation and the induced flow is expected to be minor (Beig *et al.* 2018; Zhang *et al.* 2024). Thermal effects are therefore neglected, and the flow field is governed by the Navier–Stokes equations together with the continuity equation

$$\frac{\partial \rho \boldsymbol{u}}{\partial t} + \nabla \cdot (\rho \boldsymbol{u}\boldsymbol{u}) = -\nabla p + \nabla \cdot \boldsymbol{s} + \boldsymbol{f_\delta}, \tag{2.2}$$

and

$$\frac{\partial \rho}{\partial t} + \nabla \cdot (\rho \boldsymbol{u}) = 0, \tag{2.3}$$

where t, p, ρ and $\boldsymbol{u}$ are time, pressure, density and flow velocity, respectively. Here, $\boldsymbol{s} = \mu[\nabla \boldsymbol{u} + \nabla \boldsymbol{u}^T - (2/3)(\nabla \cdot \boldsymbol{u})\mathbf{I}]$ (μ is the dynamic viscosity and $\mathbf{I}$ is the identity tensor) denotes the viscous stress tensor for the Newtonian fluid, neglecting the bulk viscosity. Concurrently, the surface tension force term $\boldsymbol{f_\delta}$ (Brackbill *et al.* 1992) is incorporated by employing the continuous-surface-force technique, expressed by

$$f_\delta = \sigma \left[-\nabla \cdot \left(\frac{\nabla \alpha_l}{|\nabla \alpha_l|} \right) \right] \nabla \alpha_l, \tag{2.4}$$

where σ is the surface tension coefficient, α denotes the volume fraction of fluids and the subscript 'l' represents the liquid.

The content within cavitation bubbles is regarded as non-condensable gases (Koch *et al.* 2016) that obey the polytropic equation of state

$$\frac{p}{\rho^\kappa} = \frac{p_n}{\rho_n^\kappa}, \tag{2.5}$$

where $\rho_n = 1.25$ Kg m^{-3} and $p_n = 101\,325$ Pa are the reference density and pressure of the gases, respectively, and $\kappa = 1.4$ is the adiabatic exponent of the gases. The liquid surrounding the bubble is modelled as a Tait-compressible liquid

https://doi.org/10.1017/jfm.2026.12123 Published online by Cambridge University Press

$$\rho = \rho_0 \left(\frac{p + B}{P_0 + B} \right)^{1/\Gamma}, \tag{2.6}$$

where $\rho_0 = 1000\ \mathrm{Kg\,m^{-3}}$ and $p_0 = 101\,325$ Pa are the reference density and pressure of liquids, $\Gamma = 7.15$ is the Tait exponent for liquids and $B = 3046$ bar is the Tait pressure.

To model the bubble dynamics, an evolution equation (Miller *et al.* 2013; Koch *et al.* 2016; Cerbus *et al.* 2022) for the liquid volume fraction is solved

$$\frac{\partial \alpha_l}{\partial t} + \nabla \cdot (\alpha_l \boldsymbol{u}) + \nabla \cdot (\alpha_l (1 - \alpha_l) \boldsymbol{U_r}) = \alpha_l (1 - \alpha_l) \left(\frac{\psi_g}{\rho_g} - \frac{\psi_l}{\rho_l} \right) \frac{Dp}{Dt} + \alpha_l \nabla \cdot \boldsymbol{u}, \tag{2.7}$$

where $\psi = D\rho/Dp$ is the compressibility term; the subscripts 'g' and 'l' denote the gas phase and liquid phase, respectively. Here, $\boldsymbol{U_r}$ is an artificial compressible term to ensure the sharpness of the bubble surface, which is calculated from the velocity difference (Rusche 2003) between the two phases.

The mass conservation equations for the two phases are written as

$$\begin{cases} \dfrac{\partial (\rho_l \alpha_l)}{\partial t} + \nabla \cdot (\rho_l \alpha_l \boldsymbol{u}) = 0, \\ \dfrac{\partial (\rho_g \alpha_g)}{\partial t} + \nabla \cdot (\rho_g \alpha_g \boldsymbol{u}) = 0. \end{cases} \tag{2.8}$$

For compressible flow, combining the two phase-continuity equations gives the mixture continuity equation

$$\left(\frac{\alpha_l}{\rho_l} \psi_l + \frac{\alpha_g}{\rho_g} \psi_g \right) \frac{Dp}{Dt} + \nabla \cdot \boldsymbol{u} = 0, \tag{2.9}$$

where ψ_l and ψ_g are the compressibilities of the liquid and gas phases, respectively.

The above equations are solved using OpenFOAM. Within the OpenFOAM framework, the pressure–velocity coupling in the momentum equation is performed using the PIMPLE algorithm (Greenshields 2015), which combines features of the pressure-implicit split-operator method and the semi-implicit method for pressure-linked equations. Here, PIMPLE is used as an iterative pressure–velocity coupling procedure within a compressible VoF formulation, and does not imply an incompressible-flow assumption. The volume-fraction equation is solved using the multi-dimensional universal limiter with explicit solution algorithm (Rusche 2015), together with an artificial interface compression term (Ubbink 1997), in order to maintain a sharp interface without geometric reconstruction. The time step is adjusted dynamically according to the Courant number to ensure numerical stability.

At each time step, the solution procedure is as follows.

(i) The VoF transport equation (2.7) is solved using the velocity field from the previous time step to update the liquid and gas volume fractions.
(ii) The mixture properties, including density and viscosity, are updated from the new phase volume fractions and the corresponding phase properties.
(iii) The momentum equation (2.2) is solved using the current pressure field to obtain the predicted velocity field.
(iv) The compressible continuity equation (2.9) is solved to update the pressure field.
(v) The predicted velocity field is corrected using the updated pressure field.
(vi) The compressibilities and densities of the two phases are updated from the equations of state, (2.5) and (2.6).

https://doi.org/10.1017/jfm.2026.12123 Published online by Cambridge University Press

Category	Setting/scheme
Pressure solver	Preconditioned conjugate gradient (PCG)/geometric algebraic multi-grid (GAMG) preconditioner with diagonal incomplete cholesky (DIC) Gauss–Seidel smoother
Velocity solver	SmoothSolver with Gauss–Seidel smoother
Volume-fraction solver	PCG with DIC preconditioner
Time derivative	Implicit Euler
Gradient	Gauss linear
Divergence – momentum convection	Gauss upwind
Divergence – volume-fraction advection	Gauss van Leer
Divergence – interface compression	Gauss interfaceCompression
Laplacian (pressure)	Gauss linear uncorrected
Interpolation	Linear

Table 1. Numerical schemes and solver settings.

These steps are repeated within the PIMPLE loop at each time step until convergence is reached, after which the simulation advances to the next time level. Temporal derivatives are discretised using an implicit Euler scheme. Convective fluxes in the volume-fraction equation are treated using a second-order van Leer scheme, whereas those in the momentum equation are discretised using a second-order upwind scheme. The remaining spatial terms are approximated using a second-order Gauss linear scheme. The main numerical schemes and solver settings are summarised in table 1.

In the numerical simulations, the boundary conditions and the number of grooves are modelled to match the experimental configuration. The top boundary, corresponding to the open/free-surface side of the experimental domain, was prescribed with the ambient pressure $p_\infty = 101\,325$ Pa, while a zero-gradient condition was applied to the velocity. On the remaining far-field boundaries, zero-gradient conditions were imposed for both pressure and velocity. No-slip boundary conditions were applied on all solid surfaces, including the groove walls and bottom surface. Owing to the symmetry of both the cavitation bubble and the groove geometry about the plane $z = 0$, only the region $z > 0$ was simulated, with the plane $z = 0$ prescribed as a symmetry boundary.

The mesh refinement is performed using a recursive cell-subdivision strategy in OpenFOAM, with layer-by-layer refinement applied in the regions of interest, as shown in figure 2. The bubble-deformation region is locally refined to a grid size of approximately 3 μm, providing more than 300 grid cells across the maximum bubble diameter. The region near the groove bottom is further refined to a spacing of 192 nm to ensure proper resolution of the boundary-layer flow. This refined near-wall region extends from $z = 0$ to $z = 500$ μm along the groove bottom. In the subsequent analyses, the resulting computational meshes contain approximately $(3\text{–}9)\times 10^7$ cells, depending on the groove width.

The rigid surfaces used in the experiments are hydrophilic. To represent this wetted-wall condition in the VoF framework, a Dirichlet boundary condition $\alpha = 1$ is imposed for the liquid volume fraction at the rigid boundaries. This treatment is appropriate for the present hydrophilic surface, but does not explicitly resolve dynamic contact angles or possible wetting transitions. In the parameter range considered here, possible contact-line effects are mainly associated with the protrusion surfaces, which are closer to the bubble and may be approached or locally contacted by the bubble interface during expansion and collapse. By contrast, the groove bottom, where the wall-shear stress is evaluated, remains separated from the bubble interface by a thin liquid film during the stages relevant to the peak shear stress. The reported wall-shear stress therefore corresponds to the liquid-phase

https://doi.org/10.1017/jfm.2026.12123 Published online by Cambridge University Press

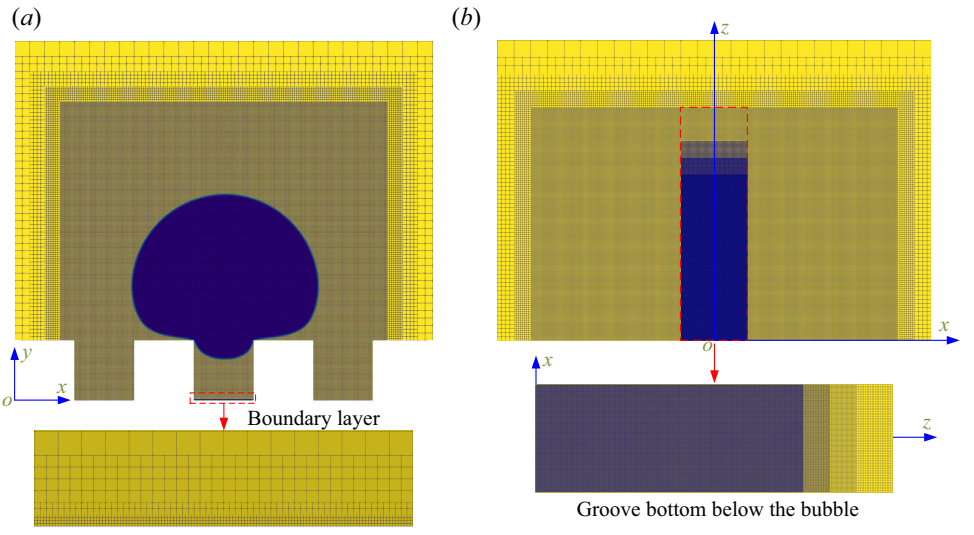


Figure 2. Mesh-refinement strategy near the groove. (*a*) Grid distribution in the $z = 0$ plane. The mesh size around the bubble is approximately 3 μm, while the region adjacent to the groove bottom is further refined to 192 nm to resolve the near-wall boundary-layer flow. (*b*) Grid distribution in the $y = 0$ plane. The 192 nm-resolution region extends from $z = 0$ to 500 μm along the groove bottom beneath the bubble.

near-wall shear induced by jet-driven spreading flow, rather than to stresses evaluated at a gas–solid contact line. More complete modelling of dynamic contact-line motion and wetting-state transitions for compressible two-phase cavitation flows remains an important topic for future work.

3. Results

In this section, we compare numerical simulations with experimental observations for two representative configurations: a bubble initiated above a groove and a bubble initiated above a protrusion. The associated jet dynamics and the resulting wall-shear flow near the groove bottom are also examined.

3.1. *Bubble initiated above the groove*

3.1.1. *Bubble dynamics*

Figure 3 illustrates the morphological evolution of a laser-induced bubble generated above the groove for $h = 171 \pm 6.2$ μm, $d = -6.2 \pm 6.2$ μm and $w = 200$ μm, corresponding to the dimensionless parameters $h^* \approx 0.37$, $d^* \approx -0.03$ and $w^* \approx 0.44$. The time of each frame, given in microseconds, is indicated in the upper-right corner. Experimental shadowgraph images are shown in the background, while the solid red lines denote the simulated bubble interface in the plane $z = 0$. In the simulations, the initial bubble radius R_0 and internal pressure P_0 are determined by matching the simulated bubble oscillation period and maximum radius with the experimental measurements (Zeng *et al.* 2020; Liu *et al.* 2026). The two parameters are fixed at $R_0 = 41$ μm and $P_0 = 100$ MPa for all subsequent simulations. During the expansion phase, the bubble base is strongly influenced by the uneven surface topography: the grooves draw the bubble downward, while protrusions locally flatten the interface. During collapse, the upper surface of the bubble accelerates downward, generating a liquid microjet directed towards the groove bottom, as observed between $t = 102$ to $t = 108$ μs. After the liquid jet impacts the lower bubble interface, most of the bubble surface is pulled into the groove. The comparison

https://doi.org/10.1017/jfm.2026.12123 Published online by Cambridge University Press

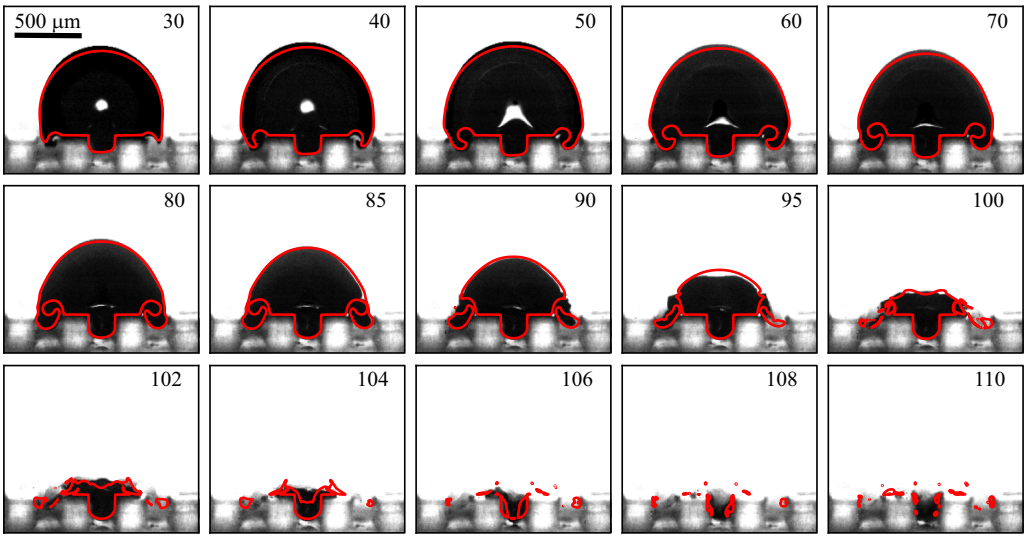


Figure 3. Comparison between experiments (background images) and simulation (red contours). Experimental images are obtained using shadowgraphy, while the simulated contours represent the bubble interface from a slice at $z = 0$. Experiment: $R_{max} = 460 \pm 6.2$ μm, $d = -6.2 \pm 6.2$ μm, $h = 171 \pm 6.2$ μm; simulation: $R_0 =$ 41 μm, $P_0 = 100$ MPa, $R_{max} = 457$ μm, $d = -5$ μm, $h = 171$ μm. The time corresponding to each frame is indicated in microseconds. The corresponding animation of the bubble dynamics is available in Movie1.avi in the supplementary movies are available at https://doi.org/10.1017/jfm.2026.12123.

in figure 3 demonstrates that, during most of the oscillation period, the computed bubble morphology well reproduces the details of experimental recordings.

Although the simulated bubble morphology agrees well with the experimental observations, local discrepancies are observed around $t = 95$ μs, where the bubble base is drawn into the adjacent grooves, causing the lateral edges of the bubble to curl inward. Accurately reproducing this behaviour would require further mesh refinement in this region, which was not pursued owing to the associated computational cost. Importantly, despite these local discrepancies, the subsequent collapse dynamics and jet-impact timing are well captured, and therefore do not significantly affect the analysis of the shear flow near the groove bottom.

While the experiments provide only shadowgraph images, which obscure information from other viewing angles, figure 4 presents both top and front views at ten selected time instants to reveal additional details of the three-dimensional bubble evolution. The bubble interface is coloured according to its height (the y-coordinate), from dark red to yellow. During the late expansion stage (see top view $t = 40$ μs), the bubble exhibits a nearly square footprint in the xz-plane while a hemispherical outline with edges and a central bottom trapped into the grooves in the front view (xy-plane). The subsequent collapse proceeds in a markedly different manner: regions near the protrusions contract more rapidly in the x- and z-directions, whereas portions confined within the grooved channel migrate slightly towards the bubble centre (see $t = 90-100$ μs). As a result, the bubble evolves into an approximately hexagonal shape, with most of its volume trapped inside the groove and only a small residual portion remaining above the protrusion surface (100–106 μs). This pronounced deformation substantially modifies the jet morphology. The liquid jet becomes slender and elongated in the z-direction (see $t = 104$ and 106 μs). After penetrating the lower bubble interface at $t = 106$ μs, the jet spreads predominantly along the groove, driving the residual bubble motion within the groove.

https://doi.org/10.1017/jfm.2026.12123 Published online by Cambridge University Press

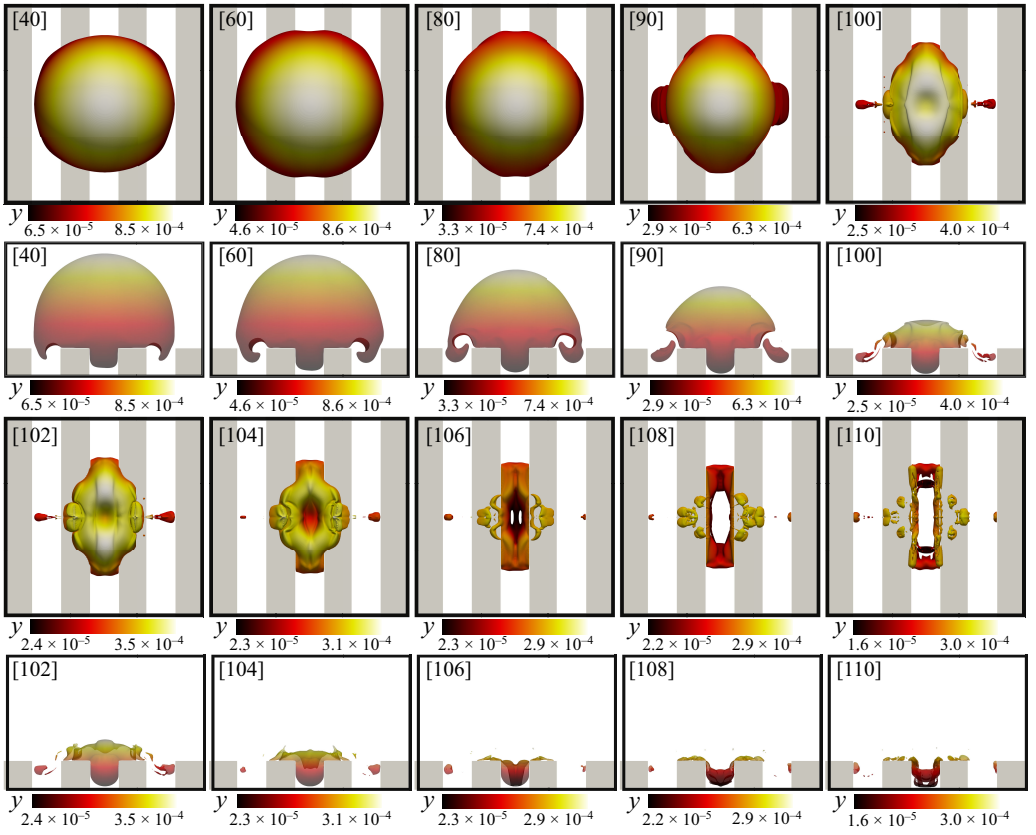


Figure 4. Bubble three-dimensional morphology for $d = -5$ μm, $h = 171$ μm, $w = 200$ μm. The first and third rows show views from the top (xz-plane), while the second and fourth rows present front views (yz-plane). The bubble surface is coloured according to its height (y-coordinate). Labels within the frames in the upper-left corner indicate the time instant in microseconds. Each frame has a width of 1400 μm. The qualitative animation of the top-view bubble dynamics is available in Movie2.avi in the supplementary materials.

3.1.2. *Shear flow and stress*

The spreading of a cavitation-induced microjet is known to generate an extremely thin boundary layer accompanied by intense shear stresses immediately after jet impact (Zeng *et al.* 2018; Gonzalez-Avila *et al.* 2020*b*). Before analysing the shear flow and wall stress in detail, we first examine the near-wall velocity profile at the location where the maximum shear stress occurs, in order to assess whether the boundary-layer flow is adequately resolved. Figure 5 compares the profiles of the velocity component u_z as a function of the wall-normal distance y for three near-wall mesh resolutions, $\Delta = 0.384$, 0.192 and 0.096 μm. The profiles are extracted at the location and time instant of maximum stress, ($x = 0$, $z = 220$ μm) and $t = 110$ μs.

Figure 5(*a*) shows that, immediately after jet impact and spreading, u_z increases from zero at the wall to a peak velocity of approximately 62 m s^{-1} within 2 μm, and subsequently decays with increasing y. Figure 5(*b*) presents a magnified view for $y < 1$ μm, where the velocity increases linearly with y. The profiles obtained with $\Delta = 0.192$ and 0.096 μm are nearly indistinguishable in both the full and near-wall views. This convergence confirms that a mesh resolution of $\Delta = 0.192$ μm is sufficient to resolve the near-wall velocity gradient while maintaining computational efficiency.

https://doi.org/10.1017/jfm.2026.12123 Published online by Cambridge University Press

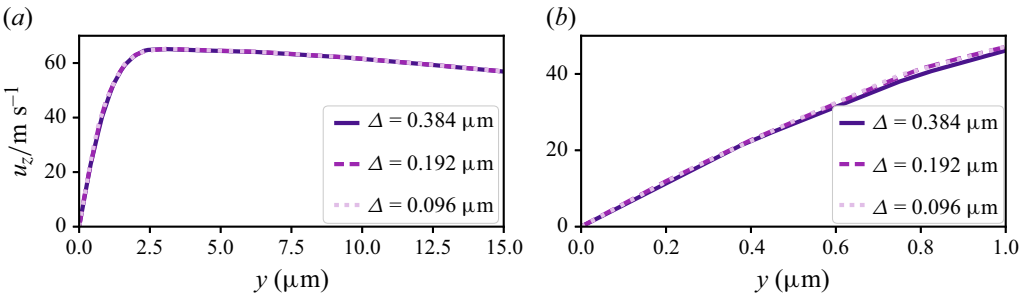


Figure 5. Grid-convergence analysis of the near-wall velocity profile at the groove bottom for three mesh resolutions, $\Delta = 0.384$, 0.192 and 0.096 μm. (*a*) Vertical profiles of the streamwise velocity component u_z as a function of the wall-normal distance y at the location and time instant where the maximum shear stress occurs, ($x = 0$, $z = 220$ μm) and $t = 110$ μs. (*b*) Zoomed-in view of the near-wall region, $y < 1$ μm, showing the linear velocity variation adjacent to the wall. The geometric parameters are $d = -5$ μm, $h = 171$ μm and $w = 200$ μm.

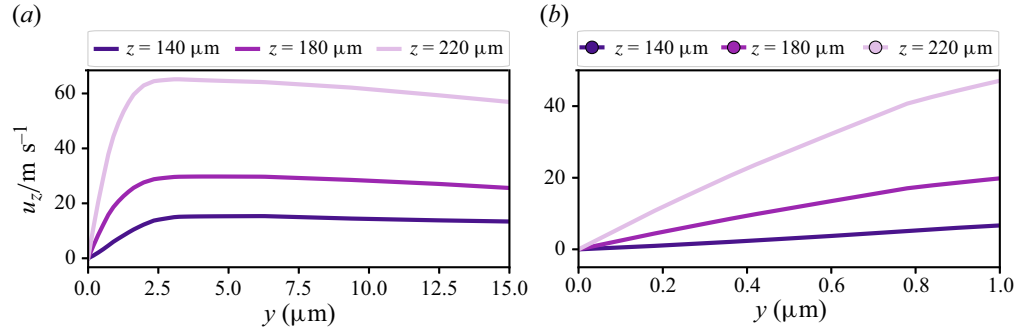


Figure 6. (*a*) Distribution of the $z-$ component of flow velocity, U_z, along the vertical direction y at $t = 110$ μs for three locations ($x = 0$, $z = 140$ μm), ($x = 0$, $z = 180$ μm) and ($x = 0$, $z = 220$ μm). (*b*) Zoomed-in view of the near-boundary region, where U_z increases linearly with y. Circular markers indicate the positions of the resolved grid cells adjacent to the wall. The geometric parameters are $d = -5$ μm, $h = 171$ μm, and $w = 200$ μm. Note the head of the spreading jet is located at approximately $z = 250$ μm.

Furthermore, figure 6 shows the vertical (y-direction) profiles of the spanwise velocity component u_z at three streamwise locations, ($x = 0$, $z = 140$ μm), ($x = 0$, $z = 180$ μm) and ($x = 0$, $z = 200$ μm) at ($t = 110$ μs) after the jet has passed. At all three locations, u_z increases from zero at the wall to a peak value and then decays, forming a boundary layer with a characteristic thickness of approximately 2.5 μm.

A magnified view of the near-wall region, shown in figure 6(*b*), demonstrates that the simulation with a fine grid resolution of $\Delta = 0.192$ μm adequately resolves the initial region of nearly constant shear adjacent to the wall. Within this region, and more specifically for $y < 0.8$ μm, u_z varies linearly with y, corresponding to shear rates of approximately 7×10^6 , 3×10^7 and 6×10^7 s^{-1} at z =140, 180 and 220 μm, respectively.

Owing to the linear variation of the shear velocity in the immediate vicinity of the wall, the wall-shear stress $\boldsymbol{\tau}$ can be directly estimated from the spatial gradient of the velocity field

$$\boldsymbol{\tau} = \mu \left.\frac{\mathrm{d}\boldsymbol{u}}{\mathrm{d}y}\right|_{y=0} \approx \mu \left.\frac{\boldsymbol{u}(y)}{y}\right|_{y\leq\epsilon}, \tag{3.1}$$

https://doi.org/10.1017/jfm.2026.12123 Published online by Cambridge University Press

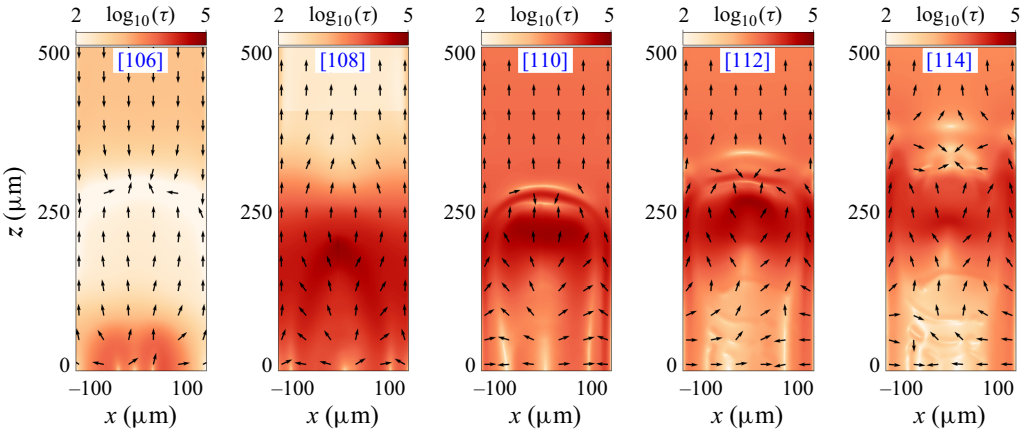


Figure 7. Wall-shear-stress distribution on the xz-plane for $h = 171$ μm, $d = -5$ μm and $w = 200$ μm. Arrows indicate the flow direction in the plane of $y = 0.2$ μm. The blue numbers denote the time instants in microseconds.

where $\epsilon = 0.2$ μm is adopted in the following analysis which lies within the linear velocity region (see figures 5 and 6) and τ has two components τ_x and τ_z in the following analysis for the two orthogonal x and z axes, respectively. In the parameter range considered here, a thin liquid film remains between the bubble interface and the grooved wall during the stages where the wall-shear stress is evaluated (Reuter & Kaiser 2019; Zeng *et al.* 2022). For a flat surface, the liquid-film thickness scales as $h_f \sim \gamma^{4.86}$ for $\gamma \leq 1.05$ and $h_f \sim \gamma$ for $\gamma > 1.05$ (see Reuter & Kaiser (2019), Zeng *et al.* (2022), Xie *et al.* (2026) for details). In more confined configurations, such as grooved structures or narrow gaps (Zeng *et al.* 2020), the liquid film is expected to be thicker because the interface motion is constrained by the surrounding geometry. The wall-shear stress is therefore calculated from the tangential velocity in the near-wall liquid-dominated region; cells containing the gas–liquid interface are not used directly in the stress evaluation. The liquid viscosity is taken as $\mu = 1.0 \times 10^{-3}$ Pa s.

Figure 7 shows the spatial distribution of the wall-shear stress on the xz-plane following jet impact. The magnitude of the shear stress is shown in red on a base-10 logarithmic scale, while arrows indicate the direction of τ (and equivalently of the near-wall velocity).

At $t = 106$ μs, the jet has just penetrated the lower bubble interface (see figures 10 and 12), generating shear stresses of the order of a few kilopascals that propagate radially outward from the bubble centre. In the remaining regions, the shear stress is approximately one order of magnitude smaller, around 10^2 Pa.

By $t = 108$ μs, after the jet has impacted and spread over a finite distance, the spreading flow becomes constrained by the channel geometry and is preferentially redirected along the z-direction. At this stage, the flow has not yet reached the sidewalls, and a high-shear region with a characteristic half-oblate shape (darkest region) is formed. The maximum shear stress reaches approximately 5×10^4 Pa at $(x = 0, z = 220)$μm.

At $t = 110$ μs, the flow component in the x-direction has reflected from the sidewalls and collides with the spreading jet, giving rise to a stagnation zone (bright region). Consequently, the dominant spreading now occurs along the groove, propagating upstream in the z-direction. A parabolic pattern of elevated shear stress develops around $z \approx 250$ μm, corresponding to the head of the spreading flow. In the following analysis, the term 'front' refers to the leading edge of the high-shear region generated by the jet-driven liquid spreading flow. As this front decelerates, the shear stress initially decreases

https://doi.org/10.1017/jfm.2026.12123 Published online by Cambridge University Press

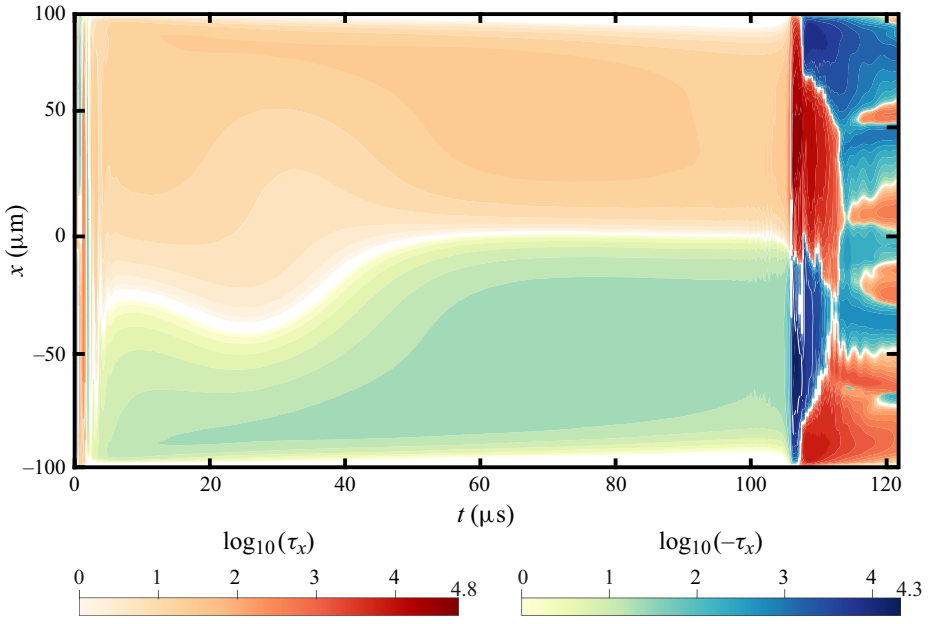


Figure 8. Spatio-temporal distribution of wall-shear stress along the x-direction on the groove bottom at $z = 0$ for $d = -5$ μm, $h = 171$ μm, $w = 200$ μm.

at $t = 112$ μs. Interestingly, a localised region of high shear stress, again reaching values of order 10^4 Pa, emerges downstream near $z = 250$ μm. This feature is associated with the interaction between the re-expanding bubble, daughter bubbles, and the spreading flow, whose combined effect generates vortex-ring-like structures that locally intensify the flow and retard the decay of shear stress (see below and Zeng *et al.* (2018)). By $t = 114$ μs, the overall level of wall-shear stress has substantially diminished; nevertheless, localised regions of elevated stress persist near $z = 250$ μm.

3.1.3. *Spatio-temporal wall-shear stress*

Next, we examine the spatio-temporal evolution of the wall-shear stress along two representative lines $z = 0$ and $x = 0$, where the maxima of the two shear-stress components τ_x and τ_z are expected to occur.

Figure 8 presents the spatio-temporal distribution of wall-shear-stress component τ_x along the groove width (the x-direction) at $z = 0$, covering the full groove width from $x = -100$ to 100 μm. Red and blue colours indicate opposite shear directions, with red corresponding to flow toward the $+x$-direction and blue toward the $-x$-direction, while white regions denote stagnation zones. During the bubble expansion phase, the stagnation zone migrates from $x = -25$ μm toward the groove centre. This asymmetry arises from a slight initial lateral offset of the bubble ($x = -205$ μm). Throughout the contraction phase, the stagnation zone remains nearly stationary at the groove centre until the formation and impact of the microjet, at which point the shear-stress magnitude increases abruptly and the stagnation location exhibits pronounced temporal fluctuations. The maximum stress in both direction reach a magnitude of the order of 10^4 Pa (dark red and blue regions). As the bubble rebounds, a reversal of the near-wall flow occurs beneath the bubble due to the competing flow directions induced by bubble collapse and subsequent re-expansion. Consequently, multiple flow-separation events develop within the groove.

https://doi.org/10.1017/jfm.2026.12123 Published online by Cambridge University Press

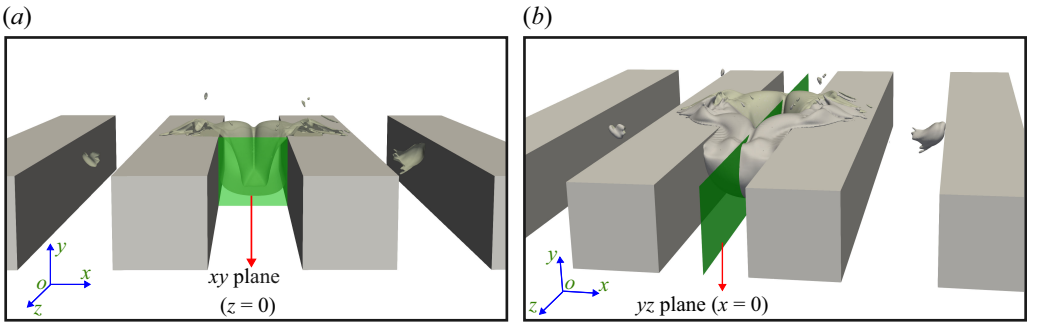


Figure 9. Schematic illustration of the cross-sectional planes. (*a*) View in the $z = 0$ plane, showing the cross-section of the bubble within the groove channel in the xy-plane. (*b*) View in the $x = 0$ plane, showing the cross-section of the bubble within the groove channel in the zy-plane.

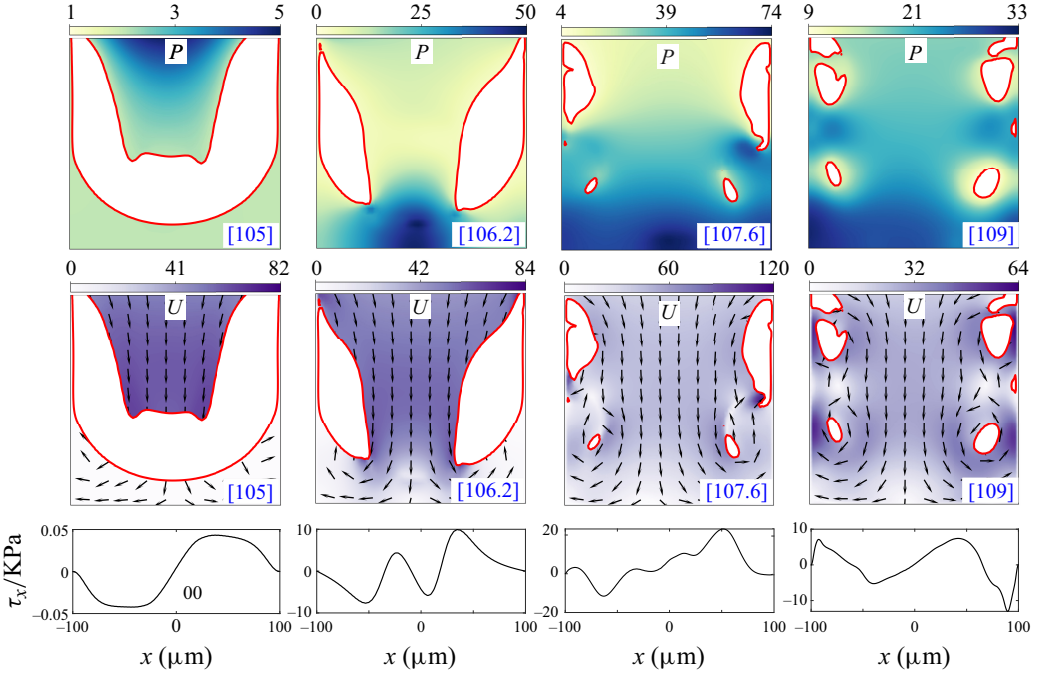


Figure 10. Pressure and flow fields in the $z = 0$ plane at four instants during jet formation and impact within the groove, together with the corresponding distribution of the x-component wall-shear stress on the bottom wall. Arrows superimposed on the velocity field indicate flow direction only. The bubble interface is outlined in red. The axes correspond to the x-(horizontal) and y-(vertical) directions, and the simulation time for each snapshot is annotated in blue (μs). The units for pressure and velocity are bar and m s^{-1}, respectively.

To further elucidate the physical mechanisms governing the spatio-temporal evolution of the wall-shear stress, the contours of pressure and velocity within the groove during the late collapse stage are analysed. In the subsequent discussions, two planes were selected for displaying the pressure and velocity distributions of the flow field (the $z = 0$ and $x = 0$ planes) to facilitate the visualisation of the three-dimensional bubble dynamics and the resulting flow fields, as shown in figure 9.

Figure 10 presents contours of pressure (first row) and velocity (second row) within the groove at four characteristic instants. These fields are shown together with the

https://doi.org/10.1017/jfm.2026.12123 Published online by Cambridge University Press

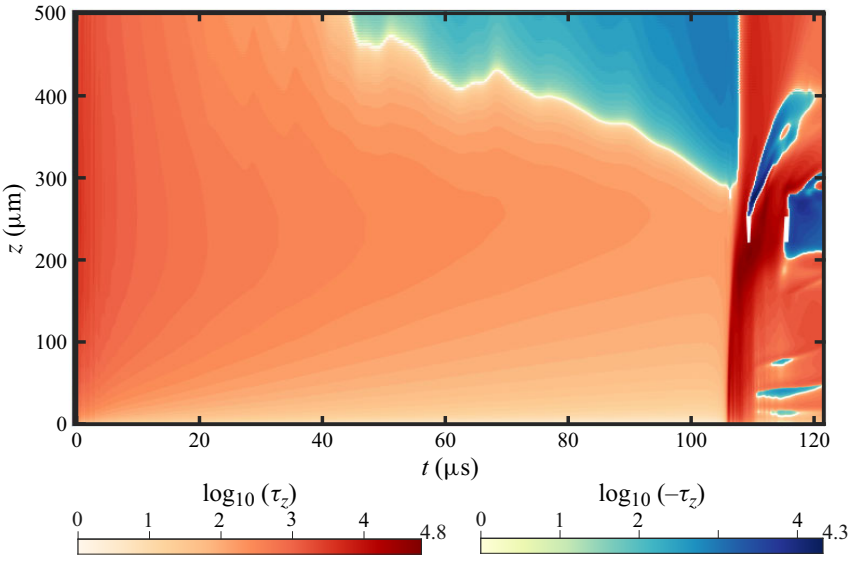


Figure 11. Spatio-temporal distribution of wall-shear stress along the z-direction on the groove bottom at $x = 0$ for $d = -5$ μm, $h = 171$ μm, $w = 200$ μm.

corresponding spatial distributions of the x-directional wall-shear stress (third row) on the xz-plane at $z = 0$.

Figures 8 and 10 jointly demonstrate that the wall-shear stress remains relatively weak, from the bubble expansion through the early collapse phase, with magnitudes of the order of tens of pascals (e.g. at $t = 105$ μs). This behaviour arises because the lower bubble interface penetrates into the groove and becomes partially trapped, thereby strongly restricting lateral flow in the x-direction and suppressing the development of significant shear stress along the wall. At $t = 106.2$ μs, a dramatic increase in shear stress occurs following jet impingement, when the jet flow spreads rapidly along the groove bottom. The maximum τ_x across the groove width is attained at 107.6 μs, reaching approximately 20 kPa. This moment is only 1.6 μs after the jet impacts the lower bubble interface at $t = 106$ μs. This peak in wall-shear stress coincides with the expansion of two toroidal daughter bubbles shed from the primary cavitation bubble. The elevated stress results from the combined effects of (i) the close proximity of the toroidal bubbles to the wall, which sustains an extremely thin boundary layer, and (ii) the spreading jet flow reaching its maximum velocity during this stage. Following this peak, the oscillatory motion of the toroidal bubbles during subsequent cycles locally reverses the near-wall flow direction beneath the bubble. This process gives rise to alternating flow separation in the x-direction, as observed around 120 μs in figure 8.

After spreading microjet reaches the groove corners, part of the liquid is redirected upward along the sidewalls (see figure 10 $t = 107.6$ and 109 μs). This upward flow, together with the oscillating daughter bubbles, generates vortical structures near the two sidewalls. The resulting sidewall-shear stress can reach approximately 60 kPa, but remains localised near the vortex region rather than forming a propagating high-shear front along the sidewall.

We now turn to the other important direction z, corresponding to the flow along the groove channel. Figure 11 shows the spatio-temporal distribution of the wall-shear-stress component τ_z along the groove length (the z-direction) at $x = 0$, spanning a wide range from $z = 0$ to 500 μm. Overall, the distribution exhibits a pattern qualitatively similar to

https://doi.org/10.1017/jfm.2026.12123 Published online by Cambridge University Press

that observed for an axisymmetrically collapsing bubble near a flat wall (Zeng *et al.* 2018). During most of the expansion phase, the shear stress within the plotted domain is positive, reflecting the outward motion of the liquid driven by bubble expansion. At larger values of z, the shear stress becomes negative as the liquid farther from the bubble centre is drawn inward, driven by the ambient pressure once the pressure near the bubble falls below p_∞. Following jet impact at $t = 106\,\mu$s, intense shear stresses rapidly develop near $z = 0$ and soon propagate along the z-direction. A peak stress of approximately 70 kPa is observed at $z \approx 200\,\mu$m and $t \approx 108\,\mu$s. The position of this peak coincides with the leading edge of the spreading flow, indicating that the maximum shear stress is closely associated with the advancing jet front. Localised regions of negative shear stress appear intermittently, arising from flow separation induced by strong adverse pressure gradients. Notably, elevated shear stresses persist around $z \approx 250\,\mu$m for a duration of approximately $10\,\mu$s, which is unexpectedly long given a characteristic spreading velocity of approximately $80\,\mathrm{m\,s^{-1}}$ from a transient jet with a duration of a few microseconds.

We next examine the detailed flow structure. Figure 12 shows contours of pressure and velocity within the groove on the xz-plane before and after the jet impact. For clarity, the symmetric region $z < 0$ is also shown.

During collapse but prior to jet impact ($t = 105\,\mu$s), liquid at larger z flows inward toward the bubble centre, following the developing jet, producing wall-shear stresses of order 1 kPa. The jet impacts the lower bubble interface at $t = 106\,\mu$s with a velocity of approximately $88\,\mathrm{m\,s^{-1}}$. Following impact, the wall-shear stress near $z = 0$ rapidly increases: it first reaches approximately 5 kPa at $z \approx 50\,\mu$m and subsequently rises by nearly an order of magnitude to approximately 50 kPa at $z \approx 200\,\mu$m as the jet spreads along the groove. The jet impingement generates a peak pressure of approximately 73 bar on the bottom wall and produces a pronounced splash, deforming the bubble interface locally into a hump at the location ahead of the spreading jet. At $t = 109.4\,\mu$s, this hump further develops as the bubble collapses, eventually splitting the toroidal bubble into two daughter bubbles. The rapid re-expansion of these bubbles drives a flow that is misaligned with the primary spreading direction, leading to the formation of vortices on either side of the jet. These vortical structures slow the decay of the spreading flow and advect the smaller toroidal bubbles closer to the wall, thereby further thinning the boundary layer. Under the combined influence of sustained high-speed flow and boundary-layer thinning, the wall-shear stress increases to approximately 60 kPa and remains localised near $z = 250\,\mu$m for an extended duration. The inward-directed shear flow remains confined to a narrow region near $z = 300\,\mu$m, which can be attributed to the vortex motion formed between the two daughter bubbles. In particular, the misalignment between pressure and density gradients gives rise to baroclinic torque (Roberts & Jacobs 2016), generating vorticity in the region separating the toroidal bubbles.

3.2. *Bubble initiated above the protrusion*

3.2.1. *Bubble dynamics*

We now turn to the second representative case, where the bubble is initiated above the protrusion of the grooved structure, in which the microjet impacts the protrusion wall, significantly altering the shear flow within the groove.

Figure 13 compares the experimental and simulation results for the conditions of $d^* \approx -1.03$, $h^* \approx 0.37$ and $w^* \approx 0.44$. Throughout the bubble dynamics, the simulated bubble profiles closely match the experimental observations. During expansion, the bottom surface of the bubble is drawn into two adjacent grooves, becoming trapped there until the later stages of collapse, when the jet penetrates the lower bubble interface. The

https://doi.org/10.1017/jfm.2026.12123 Published online by Cambridge University Press

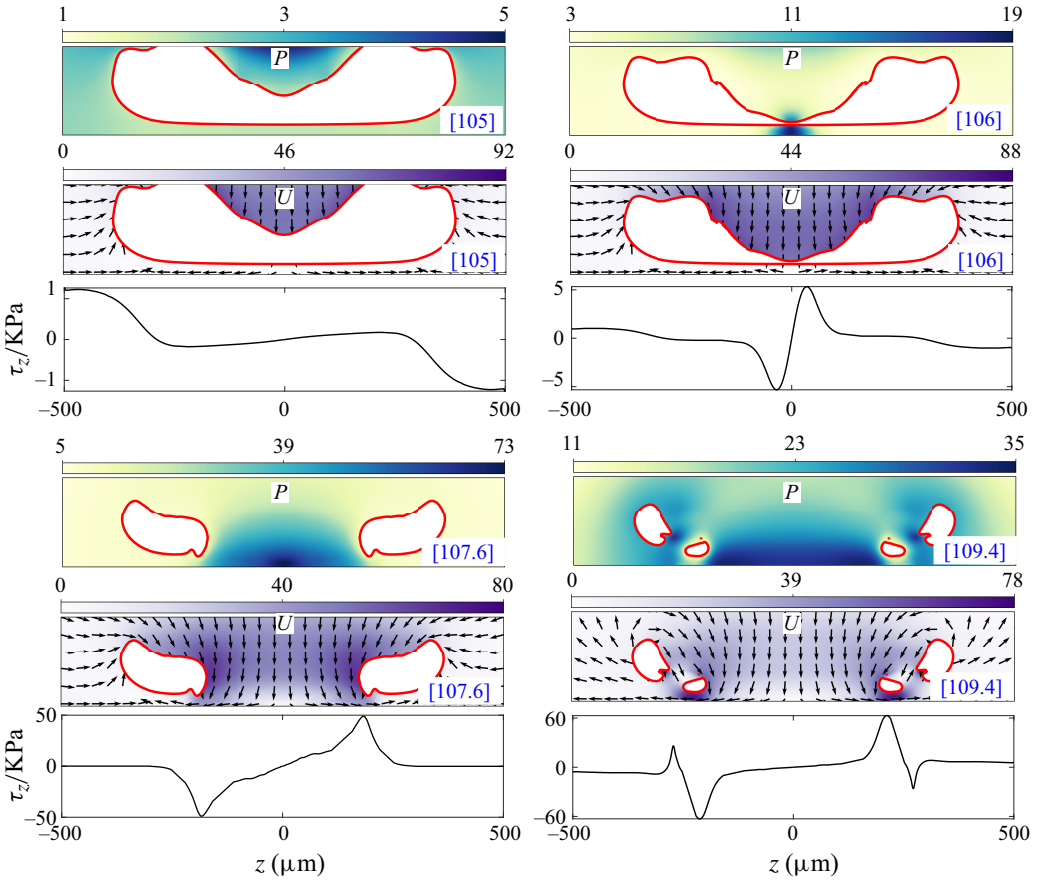


Figure 12. Pressure and flow fields in the $x = 0$ plane at four instants during jet formation and impact within the channel, together with the corresponding distribution of the z-component wall-shear stress on the bottom wall. Arrows superimposed on the velocity field indicate flow direction only. The bubble interface is outlined in red. The axes correspond to the z-(horizontal) and y-(vertical) directions, and the simulation time for each snapshot is annotated in blue (μs). The units for pressure and velocity are bar and m s^{-1}, respectively.

top surface of the bubble undergoes a typical collapse pattern, first flattening and then becoming concave, with the formation of a microjet at $t = 100\,\mu$s. The jet impacts the lower bubble interface above the protrusion at $t = 103\,\mu$s, spreading across the protrusion surface before striking the residual bubble trapped within the two adjacent grooves. This interaction induces a concave deformation in each trapped bubble, leading to the formation of a second microjet as the collapse continues. The microjets then strike the groove bottom wall at an oblique angle.

To explore the underlying fluid mechanics revealed by the two-dimensional shadowgraphy images, figure 14 presents the evolution of the three-dimensional bubble topologies from both front and top views based on three-dimensional simulation. At the initial stages of collapse, the bubble exhibits non-uniform shrinkage, with the portions above the groove collapsing faster than those above the protrusion (see top view $t = 60$ and 80 μs). This uneven motion induces kinks along the bubble interface, manifesting as ripples around the bubble at $t = 90\,\mu$s. As the interface progresses toward the location where the groove is occupied by the bubble, the direction of motion reverses, with the parts above the protrusion collapsing faster. This lateral collapse affects the vertical motion

https://doi.org/10.1017/jfm.2026.12123 Published online by Cambridge University Press

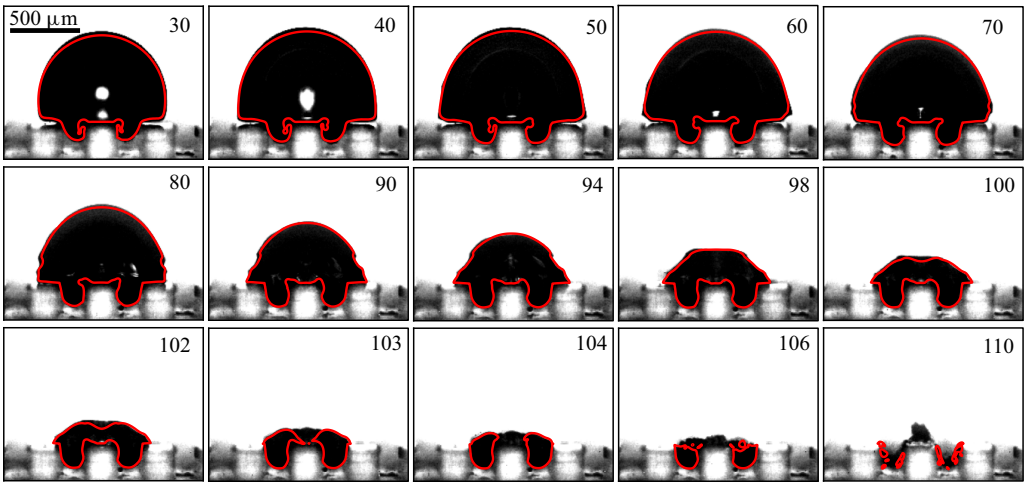


Figure 13. Comparison between experiments (background images) and simulation (red contours). Experiment: $R_{max} = 460 \pm 6.2\,\mu$m, $d = -205 \pm 6.2\,\mu$m, $h = 171 \pm 6.2\,\mu$m; simulation: $R_0 = 41\ \mu$m, $P_0 = 100$ MPa, $R_{max} = 457\,\mu$m, $d = -205\,\mu$m, $h = 171\,\mu$m. Numbers in the frames are the time in microseconds. The corresponding animation of the bubble dynamics is available in Movie3.avi in the supplementary materials.

of the bubble's top surface, leading to the formation of a square-shaped liquid jet at $t = 102\,\mu$s (see top view). After piercing the bubble, the jet adopts a quasi-square shape, which then spreads radially ($t = 104\,\mu$s). The spreading jet eventually collides with the shrinking bubble interface above the protrusion. This interaction causes the bubble to split into two square-shaped bubbles, each confined within the adjacent grooves, leaving only a small residual cluster on top of the protrusion ($t = 106\,\mu$s). The spreading jet follows the motion of the splitting interface and impacts the squared bubble inside the groove, generating obliquely downward microjets within the grooves ($t = 102\,\mu$s). At $t = 102\,\mu$s, these jets further penetrate the lower bubble interface near the groove bottom and spread, inducing significant shear flow within the groove channel.

3.2.2. *Shear flow and stress*

We next look into the detailed shear flow and wall-shear stress with the right groove. Figure 15 illustrates the spatial distribution of wall-shear stress at the groove bottom, together with the shear-flow direction during the final stage of bubble collapse, for the right groove region $-100 < x < 100\,\mu$m. In contrast to the case discussed in § 3.1, the flow field here exhibits pronounced asymmetry across the groove bottom, owing to the oblique impingement of both the expanding flow and the microjets into the groove.

At $t = 106\ \mu$s, the primary microjet from the main bubble has already impacted the protrusion and spread, whereas the secondary microjet from the trapped square bubble has not yet reached the groove bottom. At this stage, bubble contraction induces a shear flow directed toward the bubble centre. The shear stress decreases with decreasing z, and the region beneath the trapped bubble exhibits relatively low stress levels of approximately 100 Pa. At $t = 108\ \mu$s, the secondary jet impacts but not yet through the bottom surface of the trapped bubble, generating a localised high-stress region with magnitudes of a few kilopascals near $z = 0$ over the range $0 < x < 100\,\mu$m. A low-stress region appears near $z \approx 180\,\mu$m, corresponding to a stagnation zone formed by bubble fragmentation. By $t = 110\ \mu$s, the secondary microjet has pierced the trapped bubble, and the resulting shear flow propagates radially outward from the jet impingement site at approximately

https://doi.org/10.1017/jfm.2026.12123 Published online by Cambridge University Press

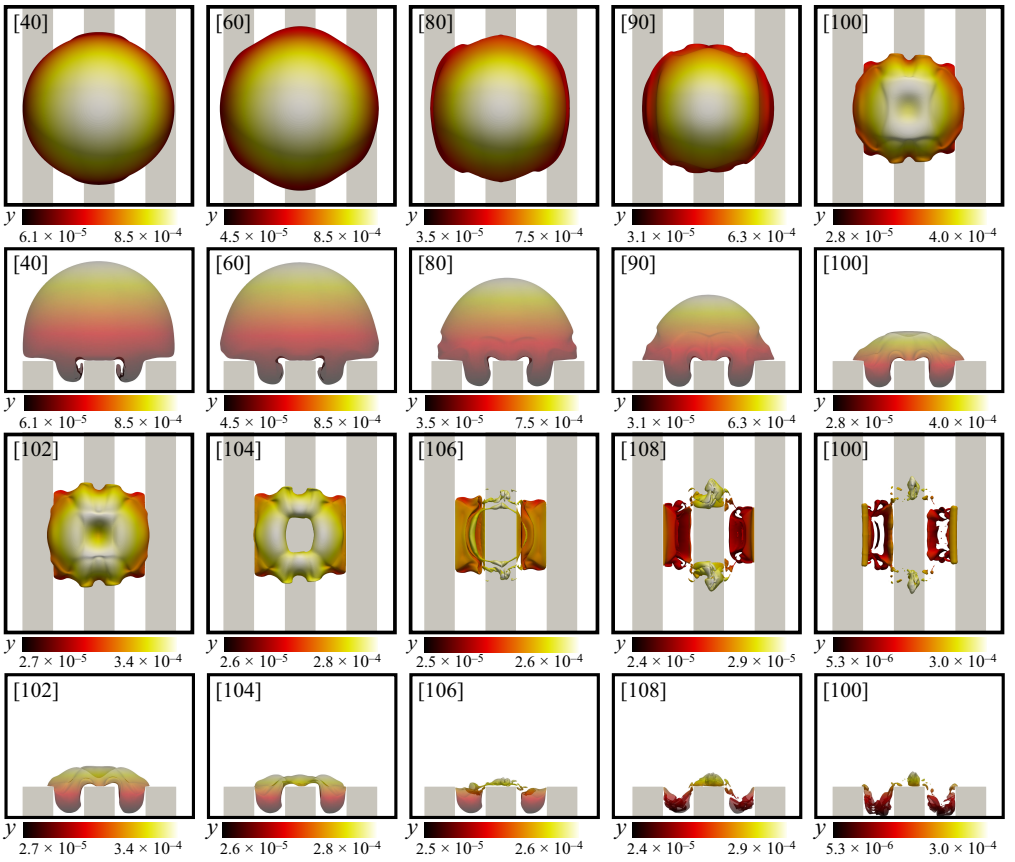


Figure 14. Bubble morphology at typical moments for $d = -205$ μm, $h = 171$ μm, $w = 200$ μm. The first and third rows display views in xz-plane, and the second and fourth rows show perspectives in the yz-plane. The bubble surface colour corresponds to the height value (y-coordinate). Labels within the frames indicate moments in microseconds. Each frame has a width of 1250 μm. The qualitative animation of the top-view bubble dynamics is available in Movie4.avi in the supplementary materials.

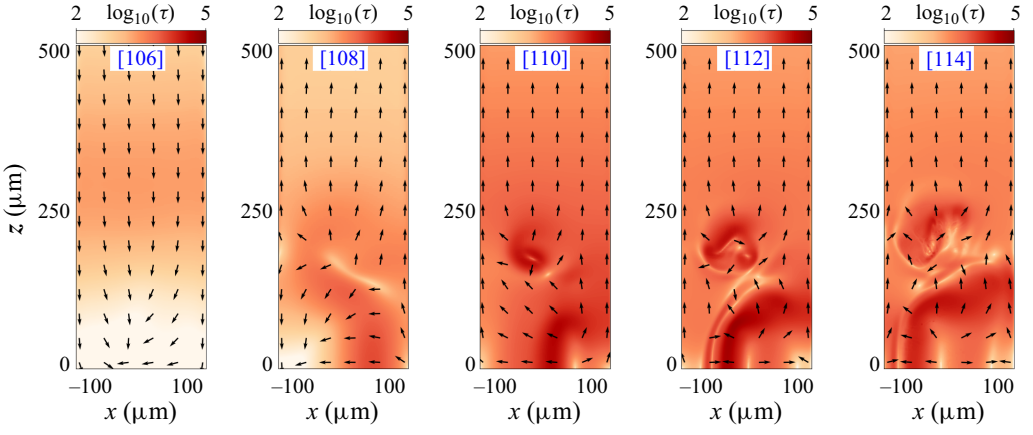


Figure 15. Spatial distribution of wall-shear stress within the xz-plane at the channel bottom for $h = 171$ μm, $d = -205$ μm and $w = 200$ μm. The arrows indicate the flow direction in the plane of $y = 0.2$ μm. The blue texts denote the moment of each panel (μs).

https://doi.org/10.1017/jfm.2026.12123 Published online by Cambridge University Press

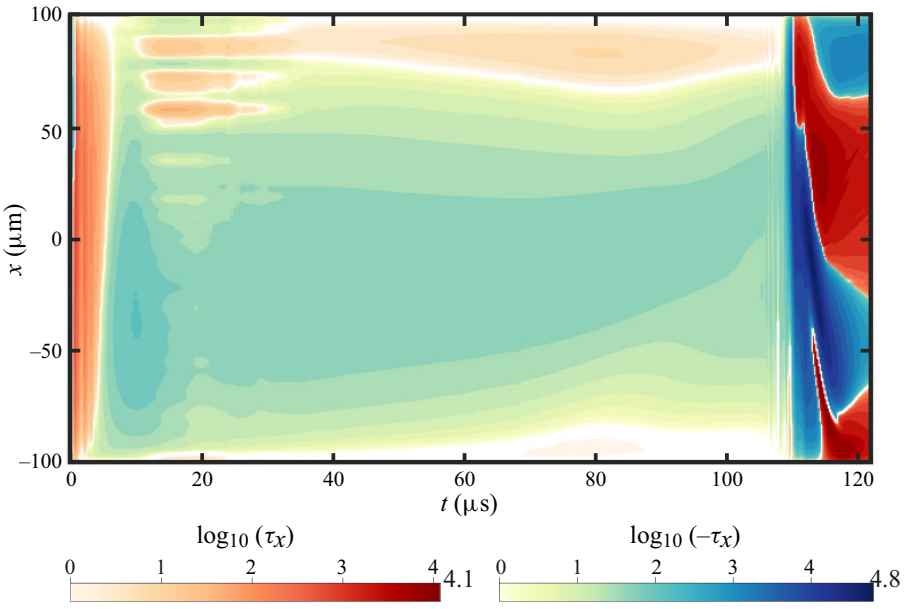


Figure 16. Spatio-temporal distribution of wall-shear stress along the x-direction on the groove bottom at $z = 0$ for $d = -205$ μm, $h = 171$ μm, $w = 200$ μm.

($x \approx 80$, $z \approx 0$ μm). High shear stresses of the order of several tens of kilopascals are generated along the spreading flow. An additional high-stress region is observed near $x = -20$ μm and $z = 180$ μm, resulting from the re-expansion of a detached bubble produced during the earlier fragmentation. This local disturbance interrupts the propagation of the shear flow along the z-direction in the range $t = 112 - 114$ μs. Meanwhile, the bubble splitting process produces multiple daughter bubbles that oscillate independently, leading to a temporally oscillatory shear-stress distribution along the z-direction. At $t = 114$ μs, the leftward flow is deflected by the sidewall and redirected along the groove channel.

3.2.3. *Spatio-temporal wall-shear stress*

Figure 16 presents the spatio-temporal distribution of wall-shear stress along the groove width (the x-direction) at the symmetry plane $z = 0$, while figure 17 shows the corresponding pressure and velocity contours within the groove at four representative instants during the formation and impact of the second jet.

During most of the bubble oscillation period, the wall-shear stresses remain below 100 Pa, indicating that the trapped bubble inside the groove effectively suppresses strong shear flow (see figure 17 $t = 106$ μs). The weak flow observed during this stage is primarily induced by bubble deformation. Initially, the shear stress is directed along the x-direction for approximately 5 μs as the bubble expands. It then reverses toward the $-x$-direction when the bubble begins to drive liquid toward the central protrusion after its lower surface is drawn into the groove. During the late collapse stage, strong shear stresses of opposite signs emerge after the second jet impacts the trapped bubble at $t \approx 109$ μs. The oblique jet impinges at approximately $x \approx 50$ μm, generating a stagnation point (white region) where positive and negative shear stresses meet. This stagnation point rapidly migrates toward the $-x$-direction following the spreading jet until $t \approx 111$ μs, then slows down.

https://doi.org/10.1017/jfm.2026.12123 Published online by Cambridge University Press

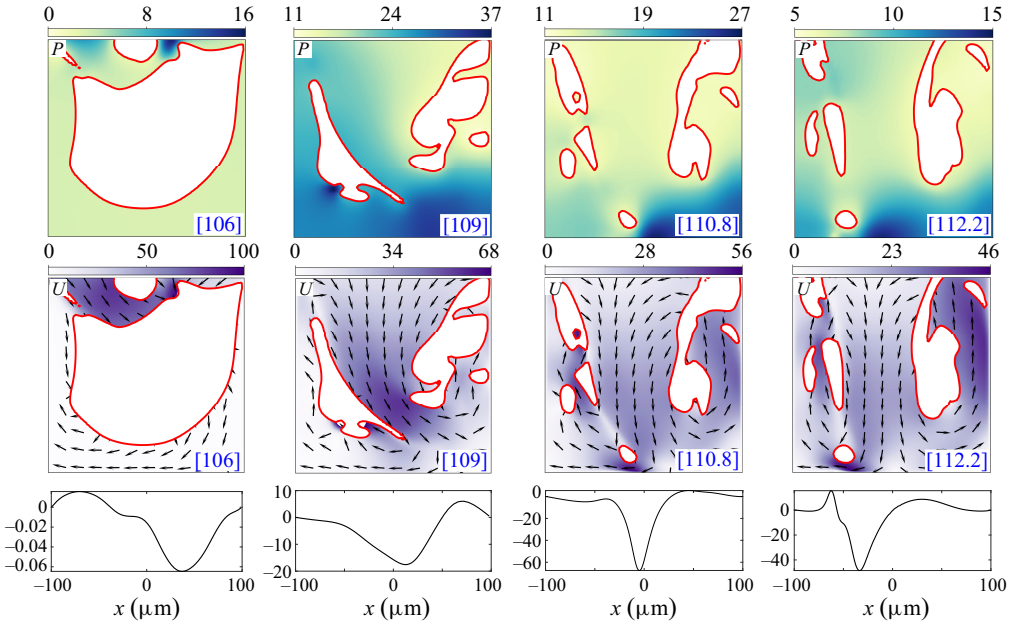


Figure 17. The bubble morphology and flow field in the $z = 0$ plane at four instants during jet penetration for $h = 171$ μm, $d = -205$ μm and $w = 200$ μm, with the corresponding temporal evolution of wall-shear stress. The first and second rows present contours of pressure and velocity inside the channel, respectively; arrows superimposed on the velocity field indicate flow direction. Row 3 plots the x-directional component of wall-shear stress as a function of x. The bubble interface is outlined in red, the axes correspond to the x- (horizontal) and y- (vertical) directions, and the simulation time for each snapshot is annotated in blue (μs).

Near the groove sidewalls, the shear stress reverses sign owing to flow reflection at the rigid boundaries.

Figure 17 provides further insight into the detailed flow fields and associated shear stress following the jet impact. At $t = 106$ μs, the oblique jet propagates inside the groove with a velocity of approximately 100 m s^{-1}; however, the wall-shear stress remains below 60 Pa because the flow is largely blocked by the trapped bubble. At $t = 109$ μs, the oblique jet pierces the bubble with a velocity of approximately 68 m s^{-1}, producing a pressure peak of approximately 37 bar near the right corner. As the jet spreads, the wall-shear stress increases to roughly 8 kPa in the $+x$-direction and 20 kPa in the $-x$-direction. The bubble then undergoes complex deformation under the combined effects of oblique jetting and collapse. At $t = 110.8$ μs, a small bubble detaches from the main bubble, compressing the boundary layer into a thinner gap and intensifying the shear stress to approximately 60 kPa in the $-x$-direction. Although the flow continues to decay as it propagates toward the groove sidewalls, the presence of vortical structures slows the decay, and the shear stress remains as high as 40 kPa at $t = 112.2$ μs. Notably, the location of peak shear stress shifts from $x \approx -5$ to $x = -35$ μm over 1.4 μs, corresponding to a propagation speed of approximately 21 m s, significantly lower than the local flow velocity of approximately 50 m s^{-1}, owing to the combined effect of the oscillation of the nearby daughter bubble and local vortex flow.

To examine the shear flow and wall-shear stress along the z-direction, we consider the central line $x = 0$ of the right groove bottom. Figure 18 shows the spatio-temporal distribution of wall-shear stress along the channel length (z-direction) at the groove

https://doi.org/10.1017/jfm.2026.12123 Published online by Cambridge University Press

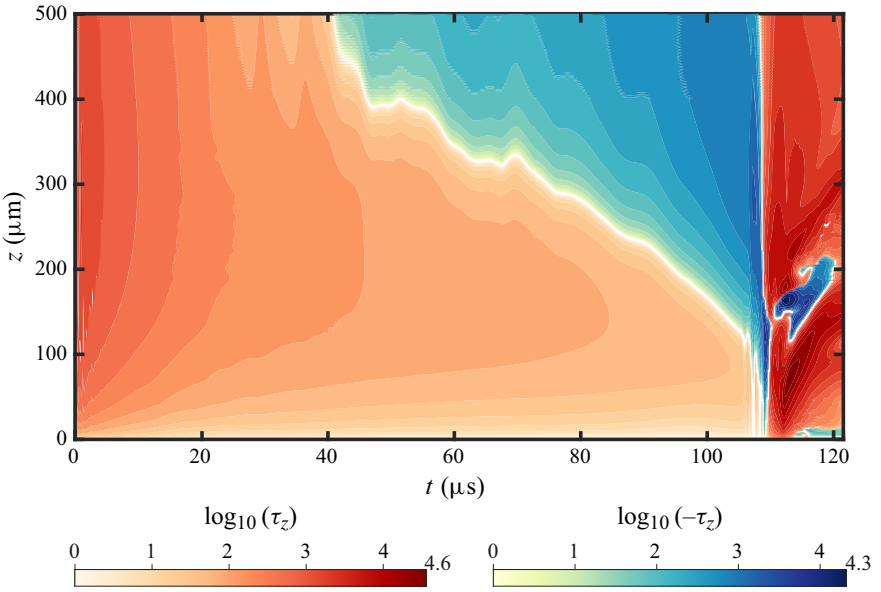


Figure 18. Spatio-temporal distribution of wall-shear stress along the z-direction on the groove bottom at $x = 0$ for $d = -205$ μm, $h = 171$ μm, $w = 200$ μm.

bottom. The overall evolution resembles that in figure 16, although the stagnation region here progressively migrates from the bubble periphery toward its centre, accompanied by an expanding region of inward-directed shear flow. During the final collapse stage, jet impact and the subsequent bubble rebound induce an abrupt flow reversal throughout the domain, resulting in positive wall-shear stress. The maximum stress in this map, approximately 60 kPa, occurs approximately 3 μs after the impact of the second microjet. During the rebound phase ($t > 112$ μs), the inward shear flow persists only near $x = 0$ and $x = 200$ μm, indicating the formation of two flow-separation regions.

The pressure and velocity fields at four representative instants on the yz-plane at $x = 0$ are shown in figure 19 to elucidate the mechanisms underlying the shear-stress distribution in figure 18. For clarity, the symmetric region $z < 0$ is also included. At $t = 106$ μs, as the primary jet propagates toward the trapped bubble, two surface depressions form owing to the presence of a small bubble near the top surface. By $t = 108$ μs, these depressions develop into jets that impinge on the lower bubble interface at $z \approx \pm 200$ μm, generating shear-stress peaks of approximately 6 kPa due to the large vertical separation between the impact location and the groove bottom. Meanwhile, the small bubble near the top collapses, and the primary jet continues to propagate toward the bubble centre, forming a second jet which is broad and fast with a width of approximately 400 μm and a downward velocity of approximately 70 m s^{-1}.

At $t = 110.8$ μs, the jet pierces the bubble and impacts the groove bottom with a velocity of approximately 38 m s^{-1}, producing a normal pressure peak of approximately 24 bar. Following jet impact, the bubble fragments into multiple daughter bubbles. The oscillations of these bubbles, together with the spreading jet, generate several shear stress peaks of approximately 20 kPa in both the $-z$ and $+z$ directions and produce four flow-separation regions. The interactions among the daughter bubbles further enhance the spreading flow, ultimately leading to a maximum wall-shear stress of approximately 50 kPa outward from the bubble centre.

https://doi.org/10.1017/jfm.2026.12123 Published online by Cambridge University Press

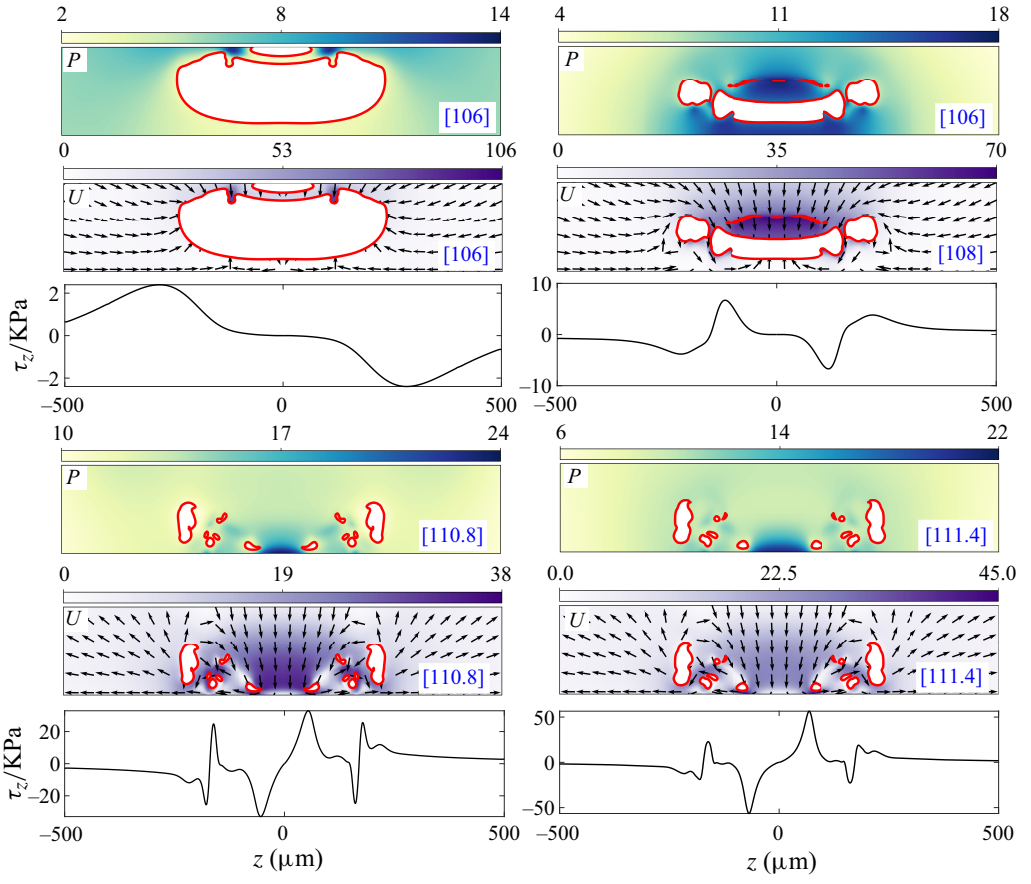


Figure 19. The bubble morphology and flow field in the $x = 0$ plane at four instants during jet penetration for $h = 171$ μm, $d = -205$ μm and $w = 200$ μm, with the corresponding temporal evolution of wall-shear stress. The first and second rows present contours of pressure and velocity inside the channel, respectively; arrows superimposed on the velocity field indicate flow direction. The third row shows the z-directional component of wall-shear stress as a function of z. The bubble interface is outlined in red, the axes correspond to the z- (horizontal) and y- (vertical) directions, and the simulation time for each snapshot is annotated in blue (μs).

4. Discussion

The above results have demonstrated that the strong shear flow at the groove bottom is intrinsically related to the impingement of the various types of microjet on the groove bottom. The formation and impact of these jets are, in turn, highly sensitive to the relative position of the bubble above the grooved structure. In this section, we therefore present a systematic parametric investigation focusing on three key parameters, namely the horizontal offset $d^* = d/w$, the vertical stand-off distance $h^* = h/R_{max}$ and the groove width $w^* = w/R_{max}$.

4.1. *Influence of horizontal position*

In this section, we examine the influence of the horizontal offset d on the wall-shear stress, while maintaining the identical initial dynamical conditions with vertical position of the bubble $h^* = 0.37$, and groove width $w^* = 0.44$, consistent with the reference configuration introduced in § 3.

https://doi.org/10.1017/jfm.2026.12123 Published online by Cambridge University Press

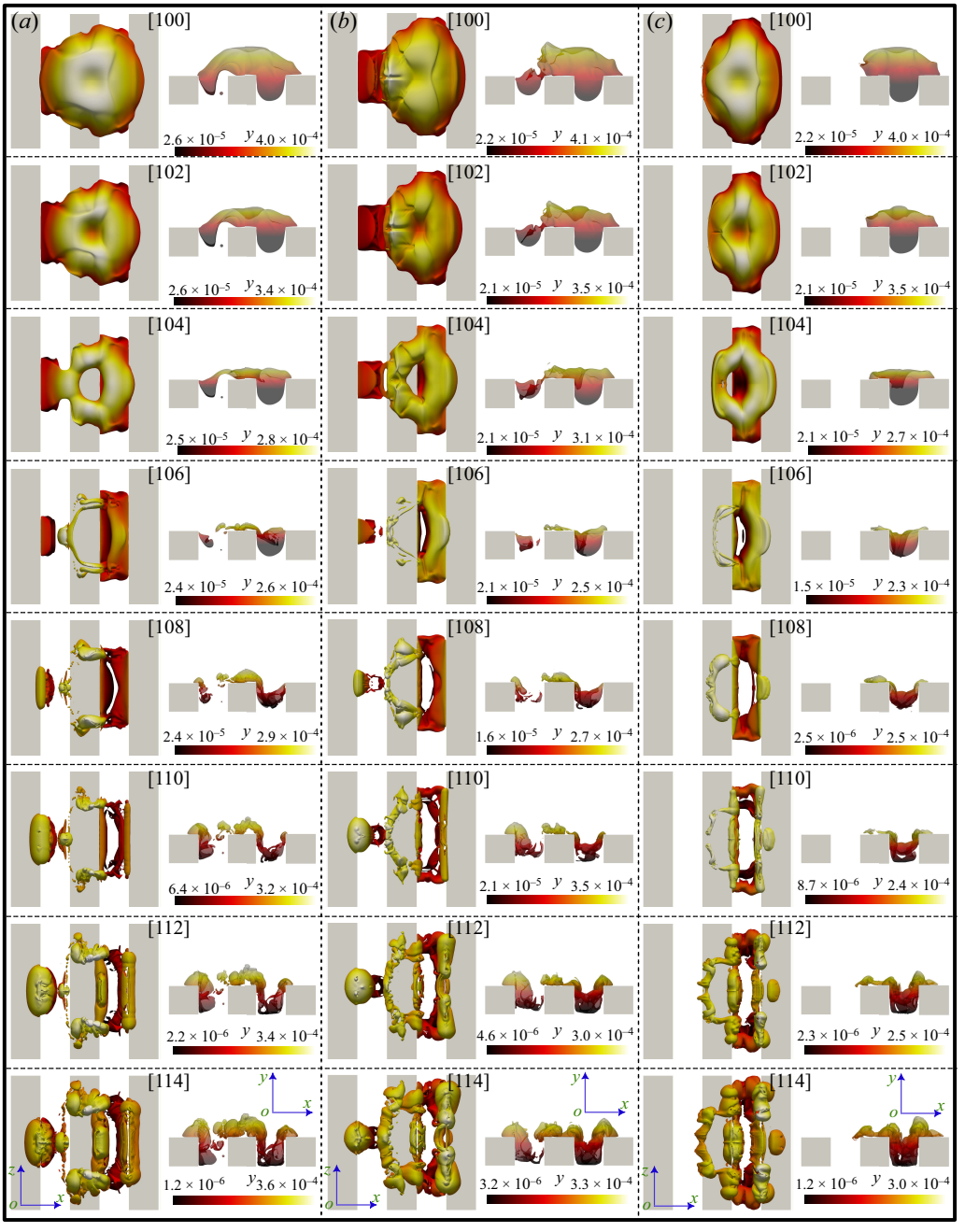


Figure 20. Dynamics of a cavitation bubble toward the end of bubble collapse situated at the same height ($h = 171$ μm, $h^* = 0.37$) and varying horizontal positions for fixed channel width ($w = 200$ μm, $w^* = 0.43$).

Figure 20 compares the simulation results for three different horizontal positions $d^* = -0.75, -0.50, -0.25$, with emphasis on the post-jet-formation stage, during which the strongest shear flow and wall-shear stress are generated. These three cases correspond to a bubble initially located above the protrusion (with a distance to the centre), above the junction between the groove and the protrusion and above the groove, respectively.

https://doi.org/10.1017/jfm.2026.12123 Published online by Cambridge University Press

As shown in figure 20, all three cases share several common features. First, the primary jet develops obliquely downward toward the centre of the protrusion. Following its first impingement, the jet spreads radially over the top surface of the protrusion, with its inner diameter gradually increasing. As the spreading flow reaches the groove edge, it is redirected into the groove channel and subsequently forms a slender, obliquely downward jet that penetrates further into the trapped bubble. These common features vanish when the horizontal offset d^* becomes sufficiently small, such that the primary jet directly impacts the trapped bubble without interacting with the protrusion, as demonstrated in § 3.1.

Varying the horizontal position d^* leads to pronounced differences in the detailed bubble dynamics, particularly in the morphology and impact location of the primary and secondary microjets, as shown in figure 20. First of all, as d^* decreases toward zero (i.e. the groove centre), the trapped bubble becomes wider in z-direction before jet impact, and the toroidal bubble moves further along the z-direction after jet spreads along the groove bottom.

When the bubble is initiated above the protrusion ($d^* = -0.75$), the primary microjet develops a half-round shape and impacts directly onto the top surface of the protrusion. Subsequently, a crescent-shaped secondary jet is generated as a result of the interaction between the spreading primary jet and the trapped bubble. As the bubble is shifted to the groove–protrusion junction ($d^* = -0.5$), the primary jet adopts a triangular shape. Its left portion impinges on the protrusion surface, while the right portion continues to move downward and pierces the lower interface of the trapped bubble, effectively acting as the secondary jet. Meanwhile, the spreading flow from the left portion of the primary jet merges with this secondary jet. Consequently, the secondary jet impacts closer to the left wall of the groove and with a less oblique incidence angle. When the bubble is further displaced toward the groove centre ($d^* = -0.25$), only a small fraction of the primary jet interacts with the protrusion, while the majority penetrates downward into the groove. In this case, the primary jet assumes a nearly half-oblate shape, and the secondary jet becomes broader.

Figure 21 presents the spatial distribution of wall-shear stress on the bottom surface of the right groove at representative instants following jet impact for the above three conditions $d^* = -0.75,\ -0.50,\ -0.25$.

First, the onset location of the outward wall-shear stress, corresponding to the impact position of the second microjet, varies systematically with d^*. For $d^* = -0.75$, the outward shear originates at approximately $x \approx 50\,\mu$m, since the second microjet is highly oblique and impacts at a position close to the right wall. At the transitional case $d^* = -0.5$, where the bubble is initially located at the groove–protrusion junction, the outward shear stress initiates at $x \approx -60\,\mu$s, reflecting the downward impact of the second jet along the left wall. When the bubble is further displaced toward the groove centre ($d^* = -0.25$), the jet impact occurs closer to the channel centreline, and the onset of outward shear shifts accordingly to $x \approx -30\,\mu$m.

The overall shear-stress distribution also depends strongly on d^*. At $d^* = -0.75$, the propagation of shear flow along the groove in the z-direction is hindered by local flow disturbances induced by bubble fragmentation and subsequent re-expansion. And the maxima stress region stays at $z < 150\,\mu$m. At $d^* = -0.50$, the coexistence of inward- and outward-directed shear flows sustains a well-defined stagnation region up to 108 μs, owing to the relatively slow contraction of the bubble. This temporal behaviour is consistent with the bubble contraction and rebound dynamics shown in figure 20. Compared with the case $d^* = -0.75$, the shear flow propagates faster along the z-direction than along the x-direction and reaches higher wall-shear-stress levels. For $d^* = -0.25$, the shear flow propagates more freely along the channel. Overall, decreasing d^* promotes faster

https://doi.org/10.1017/jfm.2026.12123 Published online by Cambridge University Press

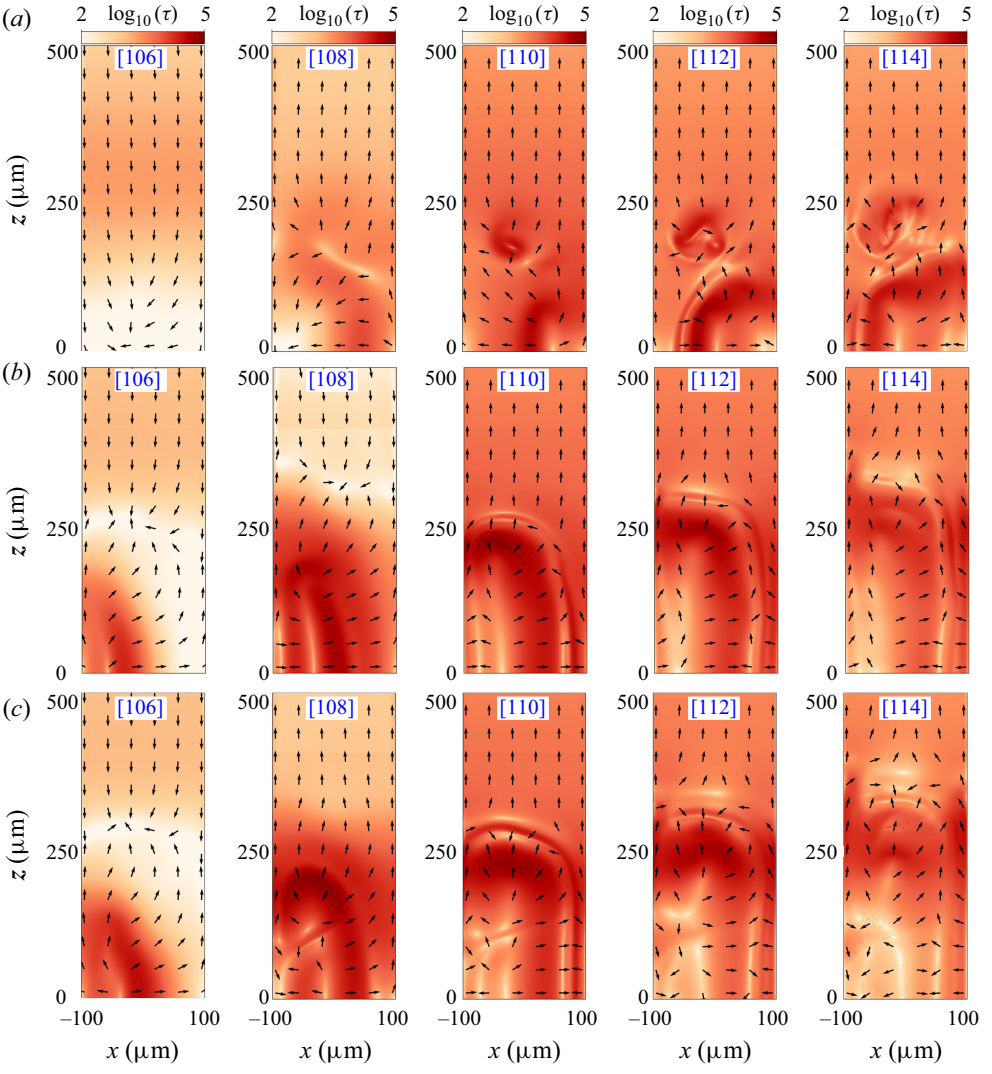


Figure 21. Wall-shear stress on the channel bottom induced by the cavitation bubble during the late stage of bubble collapse at the same height ($h = 171$ μm, $h^* = 0.37$) and varying horizontal positions for fixed groove width ($w = 200$ μm, $w^* = 0.43$): (*a*) $d = -150$ μm, $d^* = -0.75$; (*b*) $d = -100$ μm, $d^* = -0.50$; (*c*) $d = -50$ μm, $d^* = -0.25$. The blue texts indicate the moment of each image (μs). The arrows denote the direction of the shear flow.

downstream propagation of the shear flow and leads to larger amplitudes of wall-shear stress at the groove bottom.

To quantify the propagation of shear flow along the groove channel observed in the preceding figures, figure 22 presents the temporal evolution of the peak wall-shear stress τ_{max} and its corresponding streamwise location along the groove (z-direction). During the bubble contraction phase, the location of the peak shear stress migrates systematically toward the bubble centre ($z = 0$) prior to jet impact, while the stress magnitude remains small, of the order of 1 kPa. Immediately following jet impact, the peak-stress location undergoes a rapid collapse toward $z \approx 0$, after which it progressively shifts downstream as the jet spreads along the groove. Correspondingly, the peak shear stress increases

https://doi.org/10.1017/jfm.2026.12123 Published online by Cambridge University Press

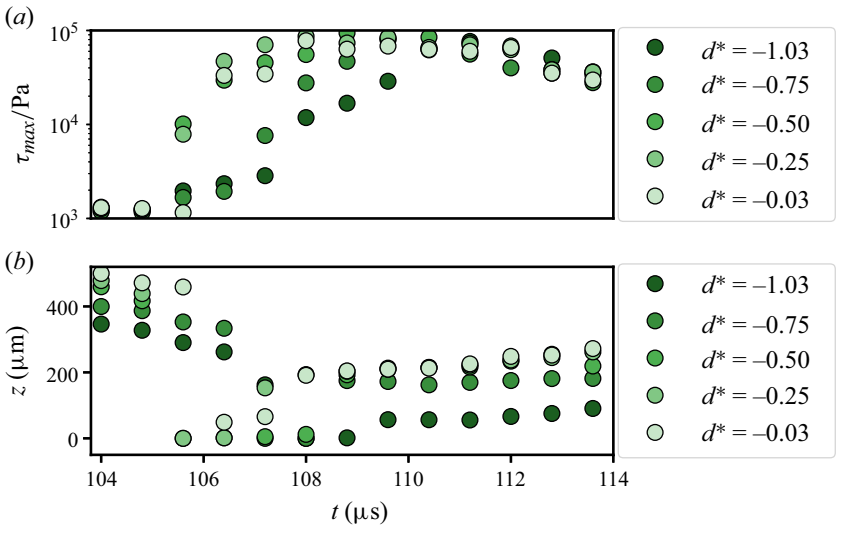


Figure 22. Temporal evolution of (*a*) the peak magnitude of wall-shear stress on the groove bottom and (*b*) its corresponding z-coordinate for $h^* = 0.37$ and $w^* = 0.43$ at various d^*. The colour of the data points, ranging from dark to light, indicates an increase in the stand-off parameter d^*.

sharply over a short interval and subsequently decays. The timing of the maximum stress is governed by the combined effects of jet spreading, flow redirection within the groove and the re-expansion of fragmented bubbles during the final stage of collapse.

As d^* increases, the peak-stress location shifts to larger z-values, with the curves converging as $d^* \to 0$. This trend indicates that the shear flow penetrates further downstream when the bubble is initiated closer to the groove centre. Indeed, for cases with $d^* > -0.5$, where the bubble is primarily located above the groove, both the peak stress and the downstream propagation distance exhibit strong similarity. In contrast, for $d^* \leq -0.5$, where the bubble is positioned near or above the protrusion, substantial differences persist among the cases.

For a bubble initiated nearly above the groove centre ($d^* = -0.03$), the shear front propagates to approximately 300 μm by 112 μs. In comparison, when the bubble is initiated above the protrusion, the shear-flow propagation is limited to approximately 100 μm. At this stage, the peak shear stress in the latter configuration has already begun to decay, reflecting the reduced efficiency of jet-driven shear transport along the channel.

4.2. *Influence of vertical position*

For a flat surface, the vertical stand-off distance is the dominant parameter governing the motion of the wall-proximal bubble interface, and thus determines the velocity and size of the resulting microjet. In the present configuration, the horizontal position is fixed at $d^* = -0.03$, and the vertical stand-off distance h^* is varied to examine its influence on the bubble dynamics and the resulting shear flow within the groove.

Figure 23 presents the three-dimensional bubble dynamics from both top and side views during the post-jet-formation stage for three representative stand-off distances $h^* = 0.25$, 0.50 and 0.75. The horizontal offset is fixed at $d^* = -0.03$ to ensure that only one microjet is formed and impacts downward on the groove surface. For all three cases, the overall collapse sequence is qualitatively similar: the lower bubble surface becomes trapped within the groove channel, while the upper surface develops into a microjet that pierces the bubble's lower interface and subsequently spreads along the channel. The

https://doi.org/10.1017/jfm.2026.12123 Published online by Cambridge University Press

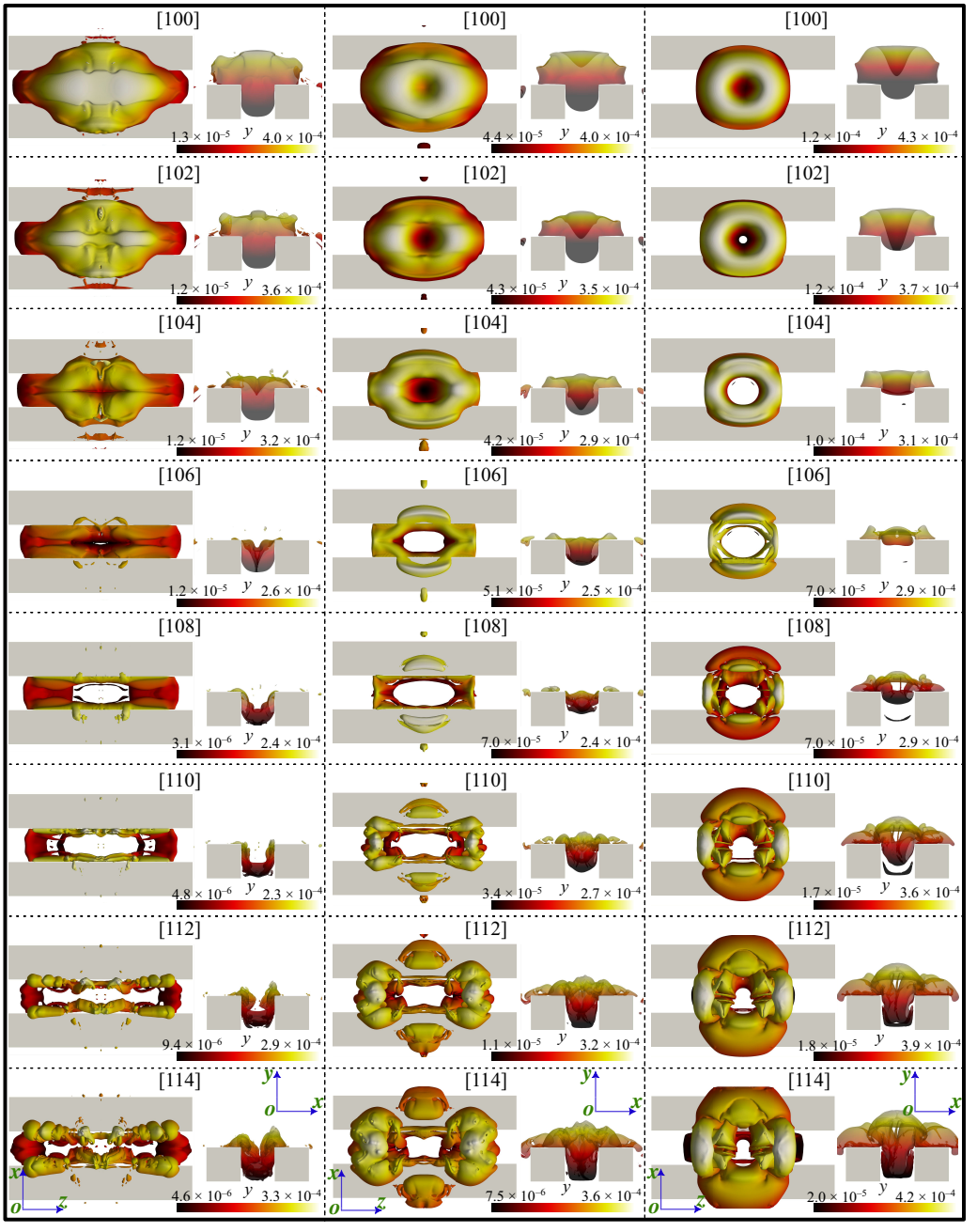


Figure 23. Dynamics of a cavitation bubble toward the end of bubble collapse situated at various heights and fixed horizontal position ($d = -5$ μm, $d^* = -0.03$) for fixed groove width ($w = 200$ μm, $w^* = 0.43$): (*a*) $h = 116$ μm, $h^* = 0.25$; (*b*) $h = 230$ μm, $h^* = 0.50$; (*c*) $h = 345$ μm, $h^* = 0.75$. The moment for each frame is indicated directly above the corresponding image (μs). The left bubble in the panels presents a view in the xz-plane, while the right bubble shows the xy-plane. The colour on the bubble surface corresponds to its y-coordinate value.

https://doi.org/10.1017/jfm.2026.12123 Published online by Cambridge University Press

corresponding jet speeds at piercing are 66.43, 56.41, 69.61 m s^{-1}, for $h^* = 0.25$, 0.50 and 0.75, respectively.

Yet the jet shapes vary significantly with the stand-off distance. At $h^* = 0.25$, the bubble develops a microjet that is slender in the x-direction but elongated along the z-direction. As h^* increases, the jet gradually becomes broader in the x-direction and shorter in the z-direction, and for $h^* = 0.75$ it approaches a nearly spherical shape. This behaviour can be attributed to the degree of confinement of the lower bubble surface within the groove. For small h^*, the bubble bottom penetrates deeply into the groove and becomes strongly trapped, which suppresses contraction in the z-direction because the trapped gas volume is distributed along the groove and exhibits limited vertical motion. Consequently, the upper bubble surface collapses more rapidly in the x-direction and impacts near the bubble centreline, producing a narrow downward depression that subsequently develops into a jet that is thin in x and extended in z.

With increasing h^*, the trapped volume decreases, and the confinement-induced retardation of z-direction contraction weakens, while the bottom surface remains farther from the groove bottom. The collapse of the upper interface along the z-direction therefore accelerates, causing the central depression to form earlier and yielding a jet that becomes broader in x and shorter in z.

The vertical jet-impact position (piercing the lower interface) also increases with h^* as the bubble becomes less confined within the groove, leading to distinct jet-spreading behaviours along the channel. For small h^*, a thin liquid layer between the bubble bottom and the groove floor inhibits vertical motion, so the lower interface primarily translates along the z-direction after jet penetration. As h^* increases, the liquid layer thickens, allowing greater vertical displacement and resulting in a reduced spreading distance of the jet along the z-direction.

Figure 24 compares the spatial distribution of wall-shear stress at representative instants for the three h^* from figure 23. Both the collapse time of the bubble and the time instant of jet impact on the lower bubble wall decrease slightly with increasing h^*. These two effects might introduce differences in the resulting shear-stress distribution.

However, the dominant factor is the thickness of the liquid layer between the bubble bottom and the groove floor, since this distance governs the jet impingement divergence: a larger separation produces a more divergent spreading flow (Phares *et al.* 2000). This effect is evidenced at $t = 106$ μs, when the jet has just reached the groove bottom. For $h^* = 0.25$, only a small region of high stress emerges near the impact site, whereas for $h^* = 0.5$ the high-stress region extends to $z = 300$ μm, and for $h^* = 0.75$ it spans nearly the entire displayed domain. In contrast to the broader distribution, the less divergent jet attains the largest spreading velocity, as shown at $t = 108$ μs, the jet front has propagated to $z \approx 250$ μm for $h^* = 0.25$, compared with only $z \approx 180$μm for $h^* = 0.5$ and 0.75.

During t =110–112 μs, the shear flow continues to propagate outward in all three configurations while simultaneously undergoing reflection from the channel sidewalls. Among the cases considered, the region of locally high velocity extends furthest for $h^* = 0.25$. In addition, the formation and motion of daughter bubbles generate local disturbances and vortical structures ahead of the spreading jet front, which inhibit flow decay and promote sustained propagation. After reflection from the sidewalls back into the channel ($t = 112$ and 114 μs), the high-stress region for $h^* = 0.25$ becomes narrower in the z-direction than in the cases h^* =0.5 and 0.75, but its magnitude is approximately one order of magnitude larger.

Figure 25 compares the temporal evolution of both the maximum shear stress in panel (a) and the corresponding z-location in panel (b) for four stand-off distances h^*. The maximum stress is approximately 140, 35, 60 and 25 kPa for $h^* = 0.25$, 0.50, 0.75 and

https://doi.org/10.1017/jfm.2026.12123 Published online by Cambridge University Press

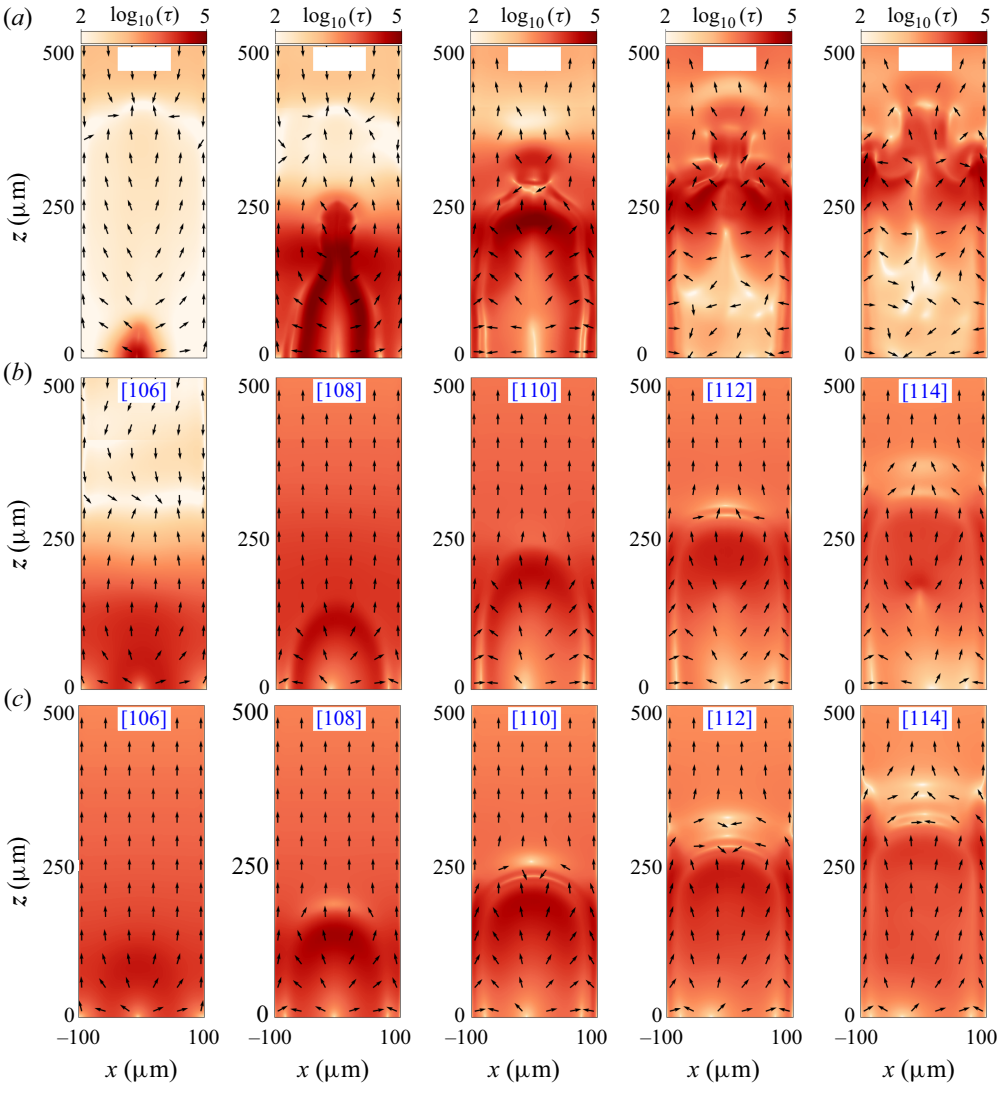


Figure 24. Wall-shear stress on the channel bottom induced by the cavitation bubble toward the end of bubble collapse situated at various heights and the same horizontal positions ($d = -5$ μm, $d^* = -0.03$) for fixed channel width ($w = 200$ μm, $w^* = 0.43$): (*a*) $h = 116$ μm, $h^* = 0.25$; (*b*) $h = 230$ μm, $h^* = 0.50$; (*c*) $h = 345$ μm, $h^* = 0.75$. The blue texts indicate the moment of each image (μs). The arrows denote the direction of the shear flow.

1.0, respectively. Among these cases, $h^* = 0.25$ exhibits not only the largest magnitude but also the fastest growth rate of wall-shear stress, highlighting the critical role of the thin liquid layer in intensifying shear at the groove bottom by confining the spreading flow. For $h^* = 0.50$, both the maximum stress and growth rate decrease as the thicker liquid layer allows the jet to spread over a wider region vertically and develop a thicker boundary layer, thereby reducing the spreading velocity (Zeng *et al.* 2022). For $h^* = 0.75$, despite the larger bubble–groove separation, the peak stress and growth rate exceed those for $h^* = 0.50$. This enhancement is primarily attributed to the re-expansion of daughter bubbles released beneath the main bubble, which further narrows the local flow passage and provides additional acceleration (see figure 23(*c*)). For $h^* = 1.0$, the jet impacts at an

https://doi.org/10.1017/jfm.2026.12123 Published online by Cambridge University Press

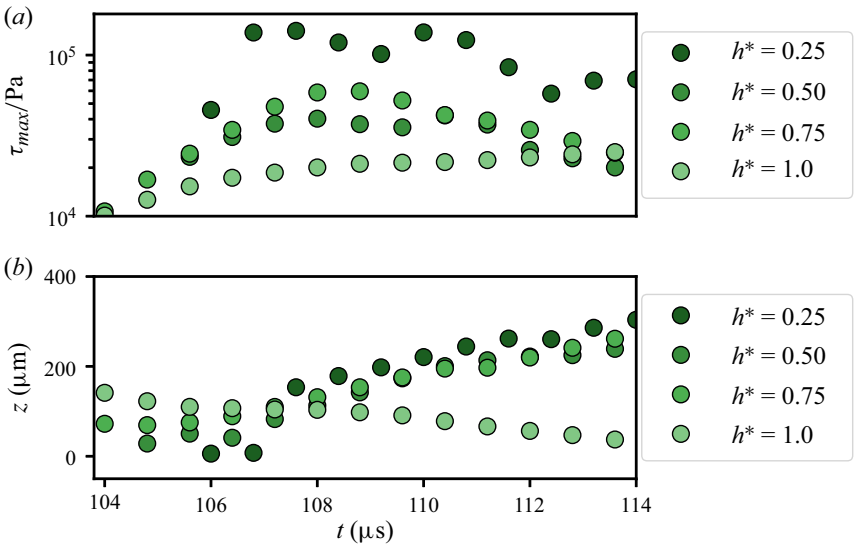


Figure 25. Temporal evolution of (*a*) the peak magnitude of wall-shear stress on the groove bottom and (*b*) its corresponding z-coordinate for $d^* = -0.03$ and $w^* = 0.43$ at various h^*. The colour of the data points, ranging from dark to light, indicates an increase in the stand-off parameter h^*.

even higher vertical position, and both the maximum stress and its growth rate decrease further.

It is noteworthy that, in figure 25, for $h^* = 1.0$, the z-coordinate corresponding to the peak stress decreases monotonically with time, while the peak stress itself increases gradually and monotonically. This behaviour contrasts with that observed in the other three configurations. To elucidate this distinctive feature, figure 26 presents the bubble morphology and pressure field distributions in the $z = 0$ and $x = 0$ planes at two characteristic instants during jet impact. Because of the large separation between the bubble and the channel bottom, the bubble remains outside the channel during jet penetration, which accounts for the substantially reduced shear stress. During the rebound stage ($t = 112$ μs), the vapour jet grows downwards and is constricted by the channel walls, producing a liquid jet flow with a relatively low velocity of approximately 40 m s^{-1} impacting the bottom (see $t = 112$ μs). As the vapour jet approaches the groove bottom, the intervening liquid layer progressively thins, enhancing flow spreading along both the x- and z-directions. Consequently, the stress peak intensifies and shifts toward $z = 0$.

4.3. *Influence of groove width*

We now examine the influence of groove width on the jet dynamics and wall-shear stress. The jet evolution for both top and front views for $w^* = 0.66$, 1.09 and 1.53 is presented in figure 27, while the remaining parameters are kept identical to those in figure 4. As w^* increases, the bubble extension in the z-direction decreases because the wider groove provides more space for lateral motion. Prior to impact, the jet morphology transitions from an elongated strip aligned with the z-direction to an elliptical shape as w^* increases.

Meanwhile, the thickness of the liquid layer between the bubble bottom and the groove surface also increases with w^*. Following jet impact (after $t = 104$ μs), the bubble extension along the z-direction further decreases with increasing w^* under the radial spreading of the jet.

https://doi.org/10.1017/jfm.2026.12123 Published online by Cambridge University Press

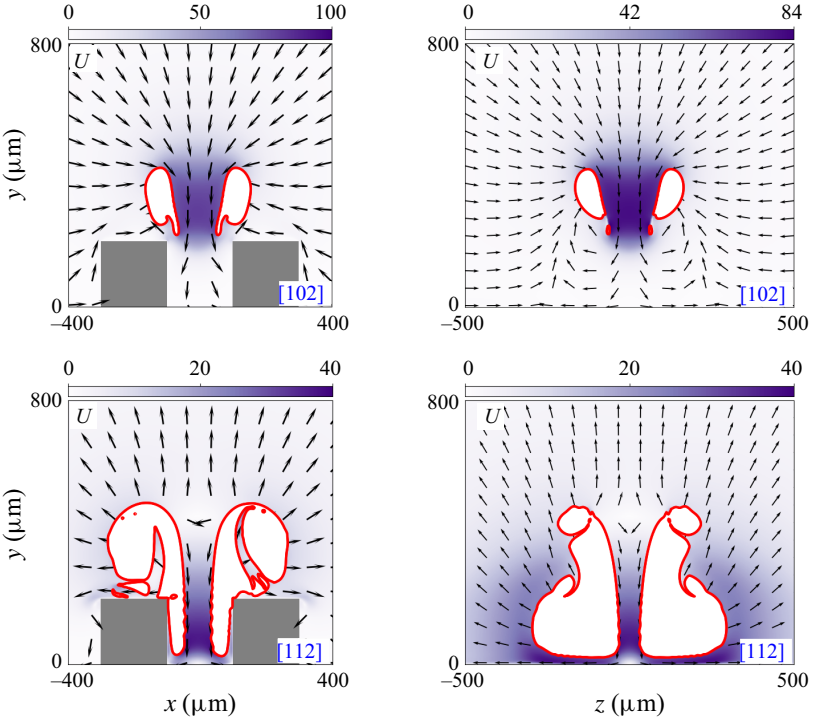


Figure 26. The bubble morphology and velocity field in the $x = 0$ and $z = 0$ planes at two typical moments for $h = 660$ μm, $d = -5$ μm and $w = 200$ μm. Flow direction is indicated by arrows. The simulation time for each frame is annotated in blue (μs).

Under both $w^* = 0.66$ and 1.09, in addition to the primary jet impact during the collapse phase ($t = 104$ μs), a second impact is observed on the lower bubble surface during bubble re-expansion from fragmented daughter bubbles ($t = 110$ μs). The xy-plane view further reveals localised bubble fragmentation along both lateral sides. For $w^* = 0.66$, the fragmented bubbles re-merge with the primary bubble during the rebound phase, whereas for $w^* = 1.09$ the separated bubbles rebound independently. When $w^* = 1.53$, the bubble becomes toroidal after the jet pierces the lower interface, and the inner diameter of the spreading jet expands radially over time.

Overall, increasing w^* weakens the confinement imposed by the channel sidewalls, leading to greater bubble elongation in the x-direction and a wider jet. Correspondingly, the fracture surface of the lower bubble during jet penetration transitions from a slender geometry to a quasi-elliptical morphology as w^* increases. In narrower channels, the liquid jet rapidly reaches the sidewalls along the x-direction and subsequently develops predominantly along the z-direction.

Figure 28 presents the spatial distribution of wall-shear stress at representative moments for w^* =0.66, 1.09 and 1.52. As the channel width increases, the propagation of the shear flow evolves toward a more uniform and radially symmetric pattern. The convergence regions of wall-shear stress correlate strongly with the jet morphology, with the localised high-stress zone closely following the front of the spreading jet after impact.

For the narrower channels ($w^* = 0.66$ and 1.09), the high-stress region exhibits an approximate walnut-shaped contour with a pronounced elongation toward larger z. When w^* becomes sufficiently large, the jet assumes a smooth elliptical form and generates a correspondingly elliptical high-stress distribution. With increasing w^*, the localised

https://doi.org/10.1017/jfm.2026.12123 Published online by Cambridge University Press

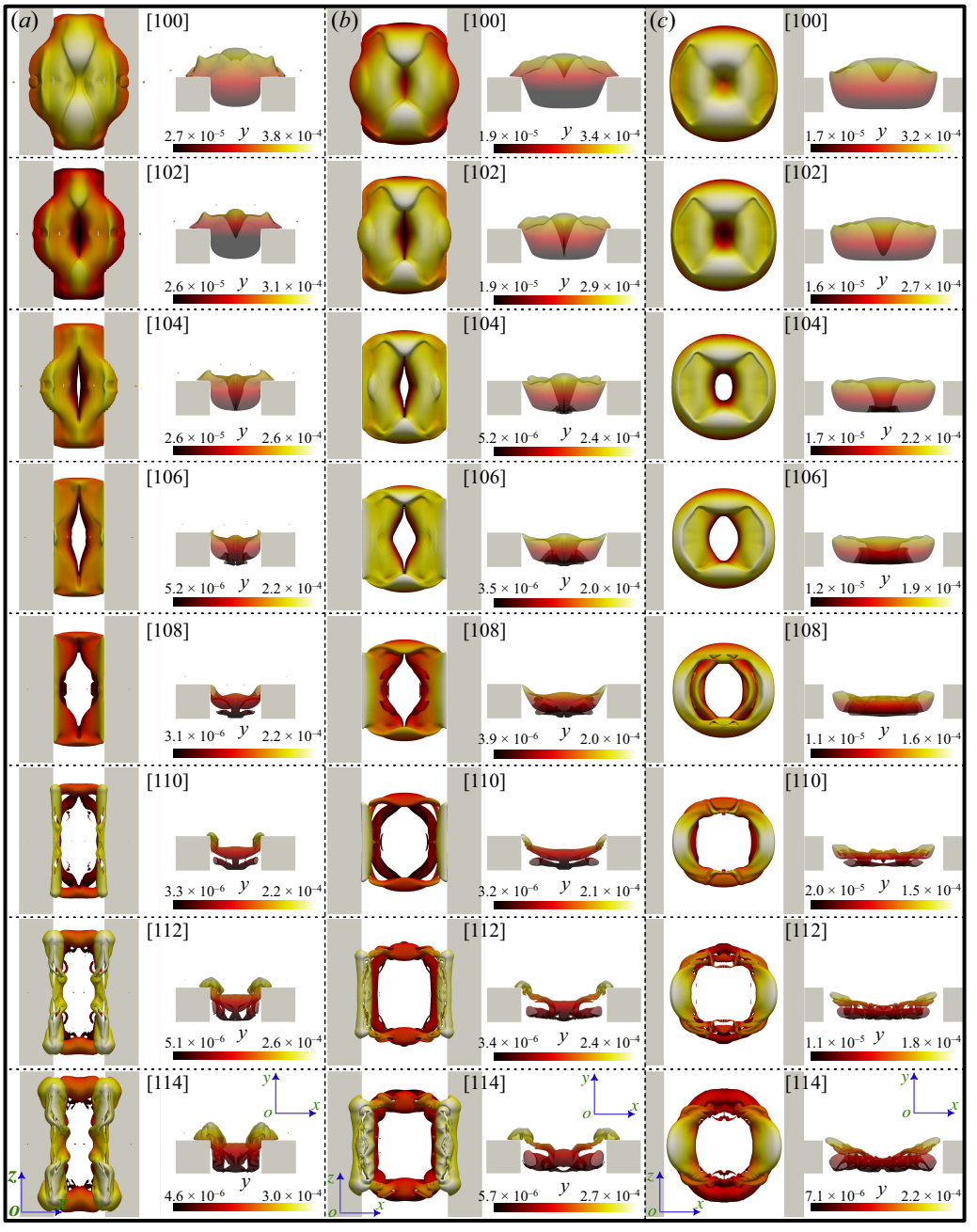


Figure 27. Dynamics of a cavitation bubble toward the end of bubble collapse situated at the same heights ($h = 171$ µm, $h^* = 0.37$) and fixed horizontal position ($d = -5$ µm, $d^* = -0.03$) for various groove widths: (*a*) $w = 300$ µm, $w^* = 0.66$; (*b*) $w = 500$ µm, $w^* = 1.09$; (*c*) $w = 700$ µm, $w^* = 1.53$. The moment for each frame is indicated directly above the corresponding image (µs). The left bubble in the panels presents a view in the xz-plane, while the right bubble shows the xy-plane. The colour on the bubble surface corresponds to its y-coordinate value.

https://doi.org/10.1017/jfm.2026.12123 Published online by Cambridge University Press

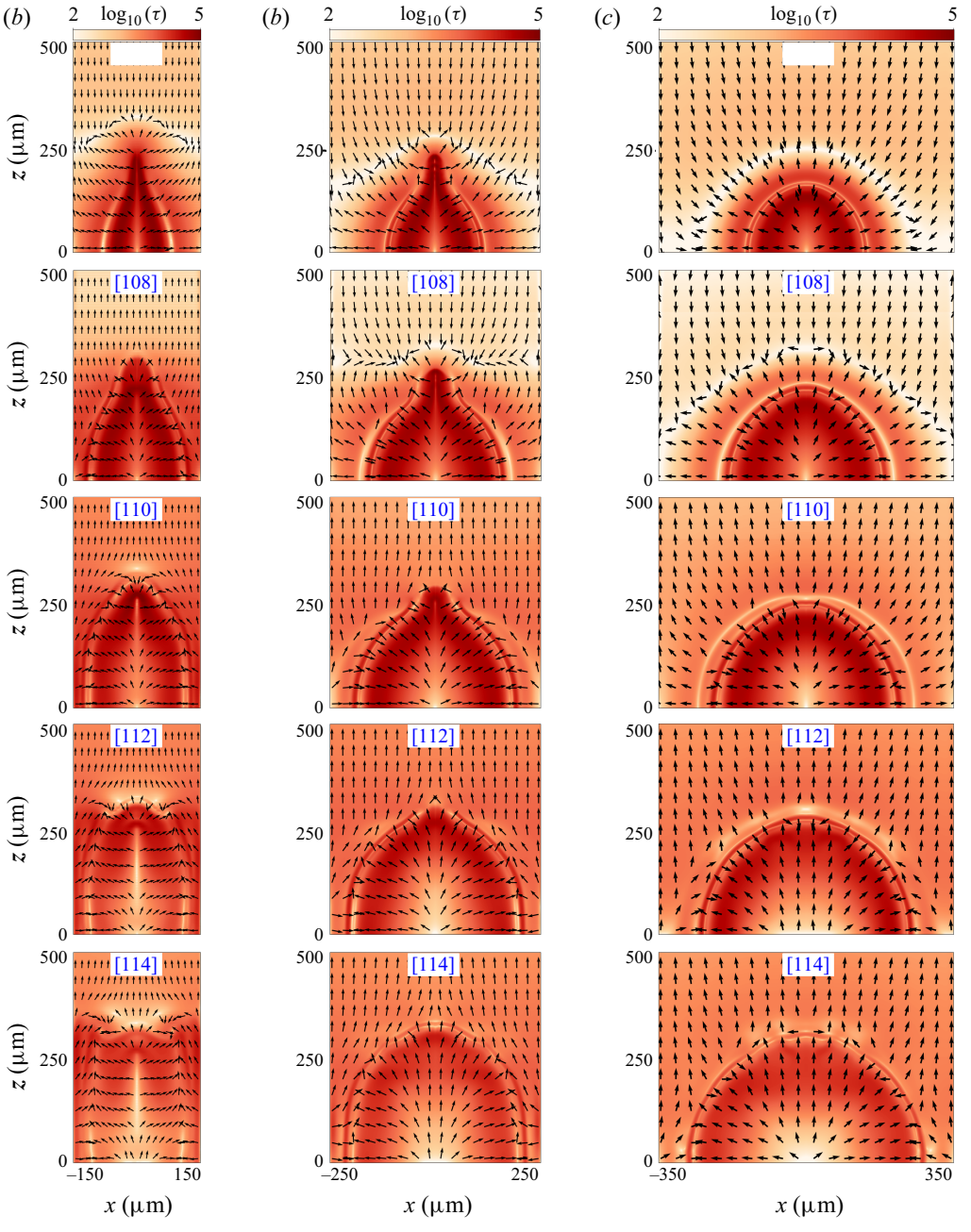


Figure 28. Wall-shear stress on the channel bottom induced by the cavitation bubble toward the end of bubble collapse situated at the same heights ($h = 171$ μm, $h^* = 0.37$) and fixed horizontal position ($d = -5$ μm, $d^* = -0.03$) for various channel widths: (*a*) $w = 300$ μm, $w^* = 0.66$; (*b*) $w = 500$ μm, $w^* = 1.09$; (*c*) $w = 700$ μm, $w^* = 1.53$. The blue texts indicate the moment of each image (μs). The arrows denote the direction of the shear flow.

https://doi.org/10.1017/jfm.2026.12123 Published online by Cambridge University Press

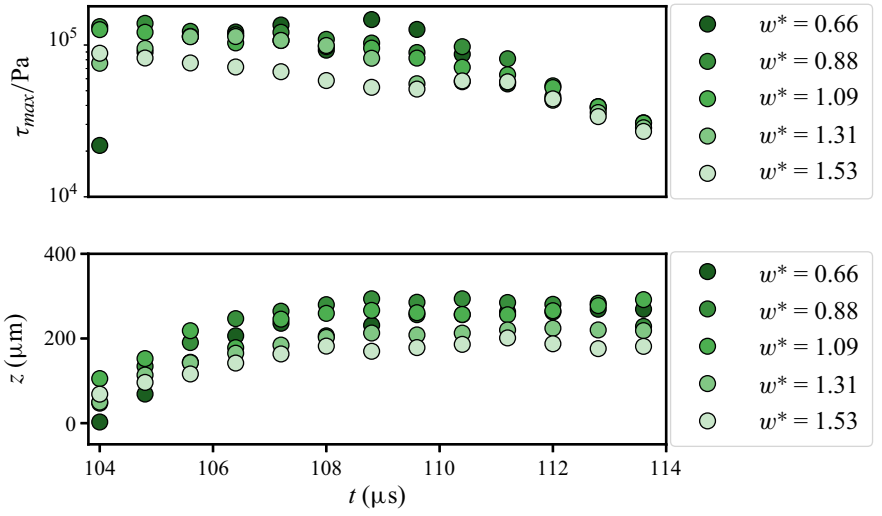


Figure 29. Temporal evolution of (*a*) the peak magnitude of wall-shear stress on the channel bottom and (*b*) its corresponding z-coordinate for $h^* = 0.37$ and $d^* = -0.03$ at various w^*. The colour of the data points, ranging from dark to light, indicates an increase in the groove width w^*.

high-stress region becomes more spatially extended but decreases in magnitude. For all cases, the shear stress exhibits fluctuations along the propagation direction, which can be attributed to bubble fragmentation and detachment.

Figure 29 presents the temporal evolution of the maximum wall-shear stress and its corresponding z-coordinate. Overall, increasing the channel width reduces both the peak shear stress and its associated z-location. A distinct behaviour is observed for $w^* = 0.66$, where the peak stress fluctuates with time, whereas for larger w^* it decays monotonically. In addition, the z-coordinate of the peak stress grows most rapidly in the $w^* = 0.66$ case. This behaviour arises from the obstruction imposed by the protrusion on the downward migration of the collapsing bubble, as illustrated in figure 28. For $w^* = 0.66$, the upper portion of the bubble is strongly constrained by the protrusion crest during collapse, while in wider channels the bubble descends more smoothly. These dynamical differences are consistent with the jet velocities measured immediately prior to jet impingement, which are 74.77, 77.68, 73.29, 68.45 and 64.41 m s^{-1} for $w^* = 0.66$, 0.87, 1.09, 1.30 and 1.52, respectively.

4.4. *Influence of surface tension*

We next examine the influence of surface tension by varying the surface tension coefficient while keeping the rigid walls hydrophilic. Three representative values are considered, $\sigma = 0.02$, 0.045 and 0.07 N m^{-1}, with the geometric parameters fixed at $h = 171$ μm, $d = -5$ μm and $w = 200$ μm, corresponding to $h^* = 0.37$, $d^* = -0.03$ and $w^* = 0.43$.

Figure 30 compares the bubble contours in the $z = 0$ plane during the late collapse stage. Surface tension affects both the morphology of the trapped bubble and the developing jet. As σ decreases from 0.07 to 0.02 N m^{-1}, the lower interface becomes flatter and more laterally extended, reflecting the weaker capillary resistance to deformation. In contrast, higher surface tension maintains a more compact interface with larger curvature and promotes a narrower trapped bubble. The jet morphology is also modified: at larger σ, the jet becomes wider and exhibits more pronounced tip oscillations, suggesting stronger coupling between jet impact and capillary-pressure-driven interfacial response.

https://doi.org/10.1017/jfm.2026.12123 Published online by Cambridge University Press

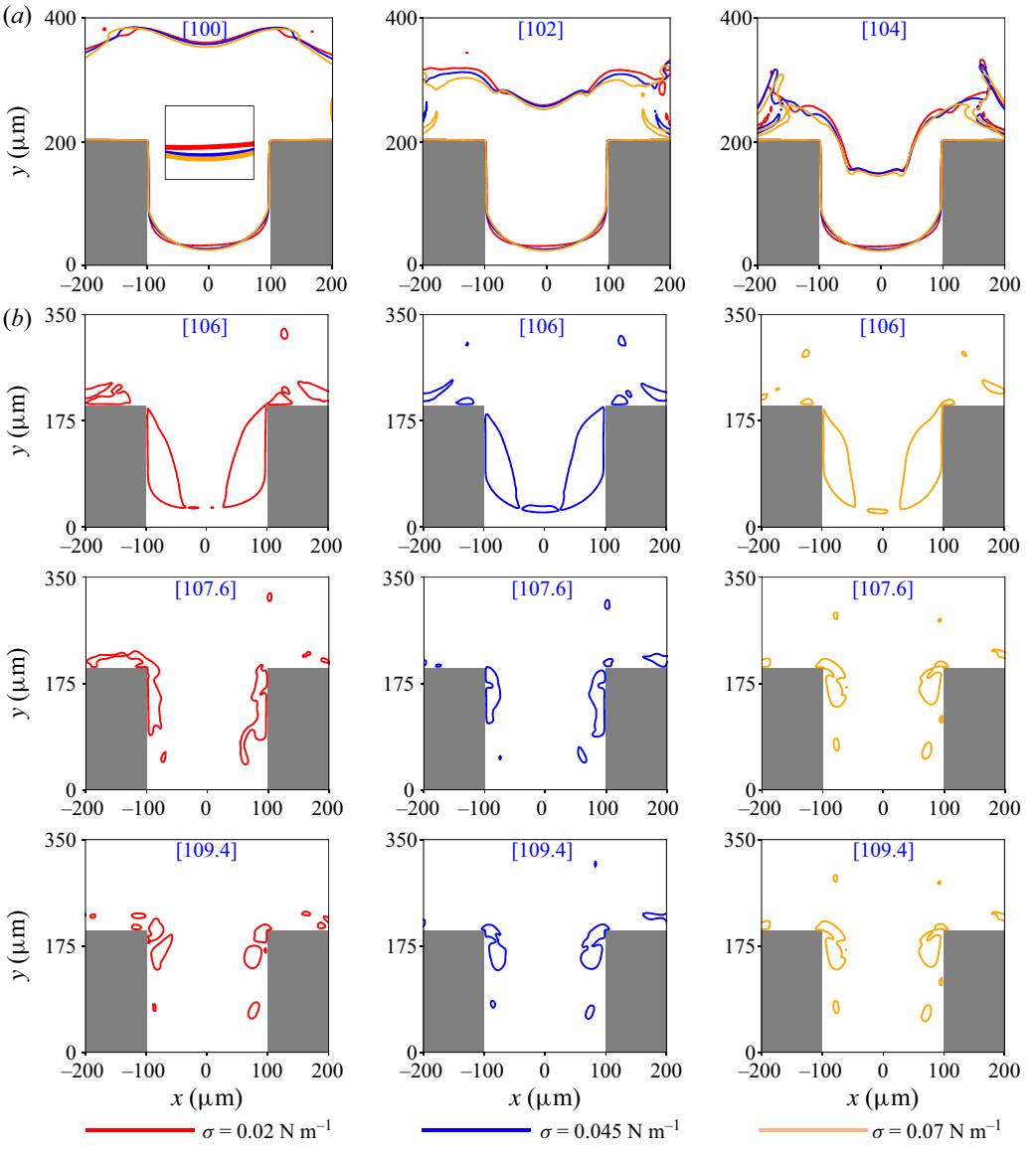


Figure 30. Bubble profiles in the $z = 0$ plane during late collapse for three surface tension coefficients, $\sigma =$ 0.02 (red), 0.045 (blue) and 0.07 N m^{-1} (orange), with $h = 171$ μm, $h^* = 0.37$, $d = -5$ μm, $d^* = -0.03$, $w =$ 200 μm and $w^* = 0.43$. The time of each frame is indicated above the image in microseconds. (*a*) Jet formation and development. (*b–d*) Bubble evolution after jet impact.

Figure 31 further shows the corresponding bubble morphology in the $x = 0$ plane and from the top view. With increasing surface tension, the bubble becomes narrower in the z-direction, while the lower interface extends further downward toward the groove bottom. This is consistent with the enhanced capillary pressure, which strengthens the restoring force associated with interface curvature and accelerates the convergence of the collapsing upper surface. After jet penetration, the detached daughter bubble also changes shape: at low surface tension it forms an elongated lip-like structure, whereas at higher surface tension it evolves into a more compact, nearly elliptical bubble. Thus, surface

https://doi.org/10.1017/jfm.2026.12123 Published online by Cambridge University Press

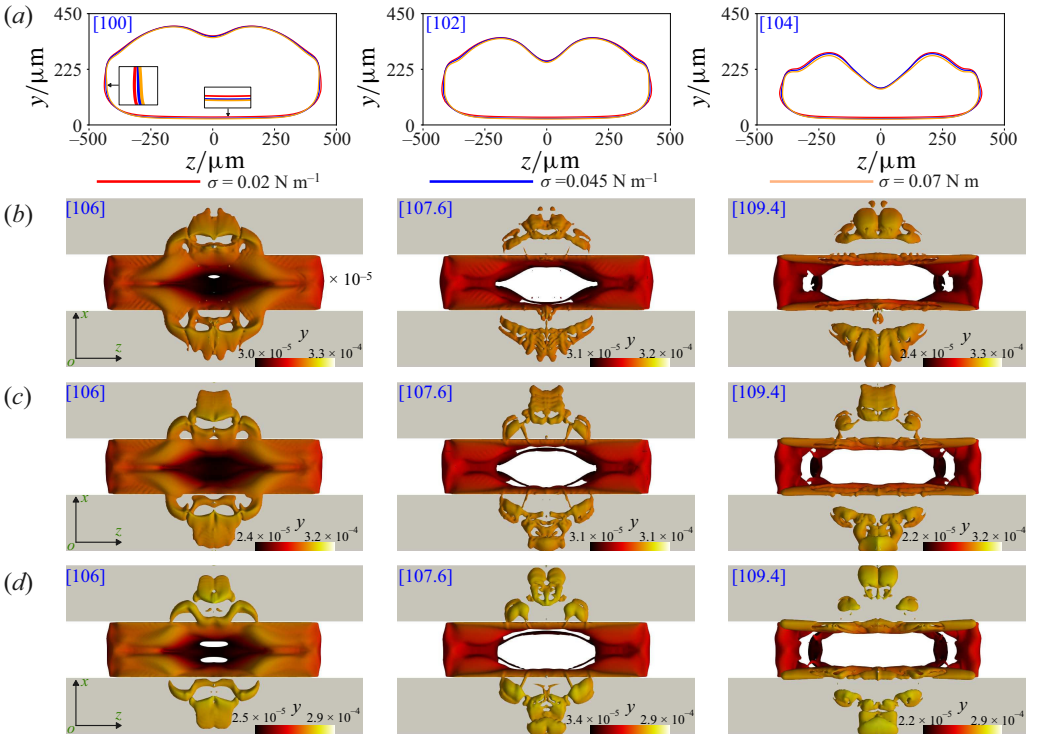


Figure 31. Bubble morphology in the zy and xz planes during late collapse for $\sigma = 0.02$, 0.045 and 0.07 N m^{-1}, with the same geometric parameters as in figure 30. The time of each frame is indicated in the upper-left corner in microseconds, and the colour on the bubble surface represents the y-coordinate. (*a*) Bubble contours in the $x = 0$ plane. (*b–d*) Top views in the xz plane for (*b*) $\sigma = 0.02$ N m^{-1}, (*c*) $\sigma = 0.045$ N m^{-1} and (*d*) $\sigma = 0.07$ N m^{-1}.

tension mainly affects the local jet-impact and fragmentation process rather than the global collapse scenario.

The corresponding wall-shear stress is quantified in figure 32, which shows the temporal evolution of the peak wall-shear stress and its associated z-location. Compared with the geometric parameters d^*, h^* and w^* discussed above, the influence of surface tension on the shear flow is relatively modest. Differences among the three cases are mainly confined to the short interval immediately following jet penetration, approximately $t = 106$–108 μs, when the jet impacts the groove bottom and daughter bubbles rapidly fragment and develop.

The maximum wall-shear stresses for $\sigma = 0.02$, 0.045 and 0.07 N m^{-1} are 83.1, 92.6 and 77.8 kPa, respectively. This trend follows the variation in jet-impact velocity, which is 52.303, 57.387 and 56.447 m s^{-1} for the three cases. The intermediate surface tension therefore produces the largest jet momentum and the strongest wall-shear stress, whereas the highest surface tension yields a smaller detached volume and lower peak stress, indicating that both impact momentum and local interface curvature contribute to the fragmentation and shear-generation process.

Despite these quantitative differences in peak stress, the downstream propagation of the shear flow is only weakly affected by surface tension. As shown in figure 32(*b*), the z-location of the peak stress follows a similar trajectory for the three cases, with noticeable deviations only shortly after jet penetration. Surface tension therefore modulates the local intensity of the wall-shear stress through its influence on jet velocity and daughter-bubble

https://doi.org/10.1017/jfm.2026.12123 Published online by Cambridge University Press

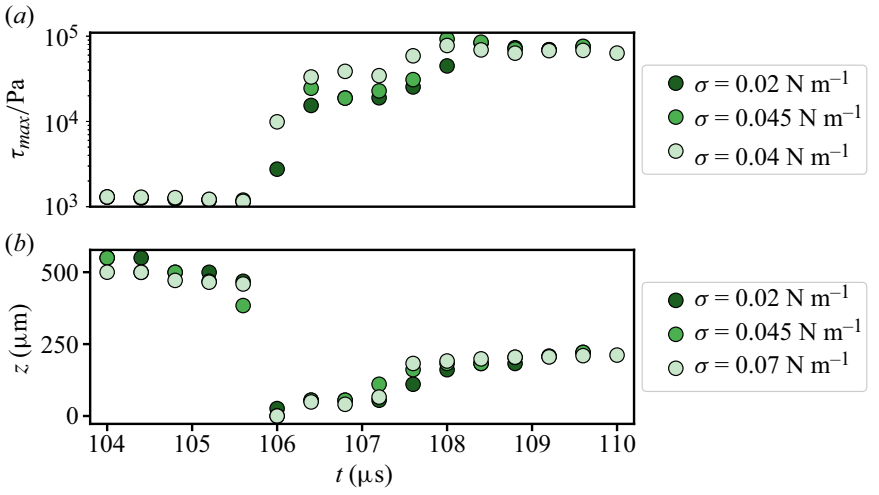


Figure 32. Temporal evolution of (*a*) the peak wall-shear stress on the groove bottom and (*b*) its corresponding z-coordinate for $h^* = 0.37$, $d^* = -0.03$ and $w^* = 0.43$ at different surface tension coefficients. The colour of the symbols, from dark to light, denotes increasing σ.

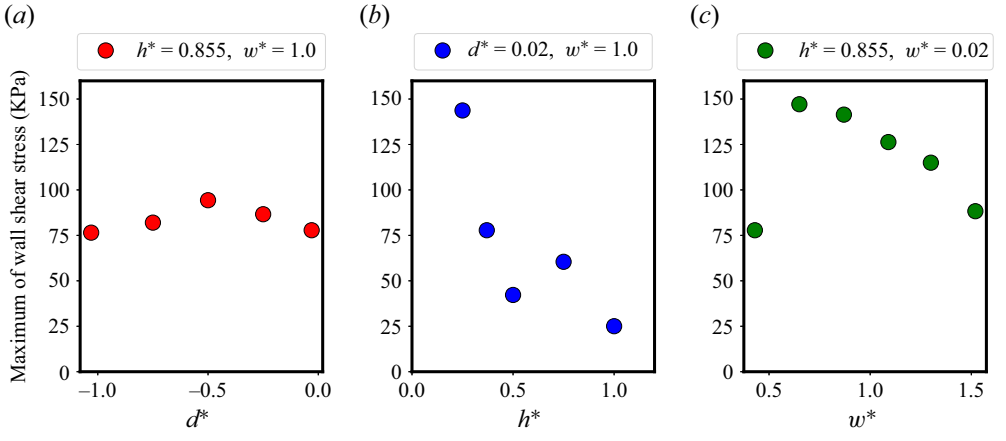


Figure 33. The summary of the spatio-temporal maximum values of wall-shear stress across all cases in this study. The red, blue and green circles represent the spatio-temporal maximum of wall-shear stress with respect to d^*, h^* and w^*, respectively.

fragmentation, but does not substantially alter the overall spreading of the shear flow along the groove.

4.5. *Comprehensive discussion on the maximum wall-shear stress*

The preceding analysis indicates that the wall-shear stress is governed by three primary flow processes: the spreading of the jet, flow refocusing induced by the groove sidewalls and the re-expansion of daughter bubbles. These mechanisms are strongly coupled to the three geometric parameters d^*, h^* and w^*. We therefore provide a comprehensive discussion on how these parameters influence the maximum wall-shear stress. Figure 33 presents the peak spatio-temporal wall-shear stress as a function d^*, h^* and w^*, shown in panels (*a*), (*b*) and (*c*) respectively.

https://doi.org/10.1017/jfm.2026.12123 Published online by Cambridge University Press

Figure 33(*a*) shows that the horizontal bubble position exerts a relatively weak influence on the maximum spatio-temporal wall-shear stress. As d^* increases, the peak stress first rises and then decreases, attaining its maximum when the bubble is initiated directly above the channel sidewall, where the jet becomes more strongly focused (see § 4.1). Across the full range of inception locations – from above the channel to above the protrusion – the variation in maximum spatio-temporal shear stress remains within approximately 25 kPa.

The initial bubble height exerts the most pronounced influence on the maximum spatio-temporal wall-shear stress, as shown in figure 33(*b*). In general, the peak shear stress decreases with increasing h^*, except for $h^* = 0.75$, where a secondary increase occurs due to the strong re-expansion of fragmented daughter bubbles enhancing the boundary flow spreading, as discussed in § 4.2. An increase in h^* from 0.25 to 1.0 reduces the maximum spatio-temporal shear stress by approximately 120 kPa, underscoring the dominant role of the bubble–wall separation in determining the shear-stress intensity.

Figure 33(*c*) shows that the maximum spatio-temporal wall-shear stress first increases to approximately 150 kPa and then decreases with increasing w^*. As the groove width increases from 0.43 to 1.52, the resulting peak shear stress varies by approximately 75 kPa, attaining its maximum near $w^* = 0.66$. In a relatively narrow channel $w^* = 0.43$, the protrusion hinders the downward migration of the bubble, thereby weakening the influence of bubble collapse on the near-bottom flow. In contrast, in wider channels, the reduced lateral confinement allows the jet to spread more freely along the groove width, which in turn alleviates the shear-flow intensity in the z-direction.

5. Conclusion

In summary, this study combined a three-dimensional compressible VoF solver and ultrafast photography to numerically and experimentally investigate the shear flow and wall stress induced by cavitation-bubble jets near grooved structures.

We first compared the computed bubble dynamics with experimental observations for two representative configurations, namely a bubble initiated above a groove and above a protrusion. In both cases, the simulations accurately reproduced the experimentally observed bubble deformation and jet evolution. Based on the validated numerical results, a two-stage jet-formation mechanism was identified for a bubble initiated above a protrusion: the distal bubble surface first develops a primary microjet that may impact the protrusion and subsequently spreads into the trapped bubble, thereby generating a secondary jet that pierces the lower bubble interface near the groove bottom.

Following jet impact, the maximum wall-shear stress at the channel bottom occurs close to the impact instant. Most peak stresses arise from the initial rapid jet spreading, while the remaining maxima are associated with secondary acceleration during bubble re-expansion. The direction of the wall-shear flow is primarily governed by the jet-impact location, but is further modulated by bubble fragmentation and vortex motion produced by the interaction between bubble re-expansion and the fast spreading jet.

When the bubble is initiated above the groove, the wall-shear stress in the z-direction (along the channel length) is significantly greater than that in the x-direction (across the channel width). In contrast, when the bubble originates above the protrusion, the oblique jet impact inside the channel enhances shear-flow propagation in the x-direction, leading to a pronounced increase in the x-component of wall-shear stress.

https://doi.org/10.1017/jfm.2026.12123 Published online by Cambridge University Press

A systematic parametric study was further conducted to discuss the influence of three key geometric parameters: the horizontal offset d^*, the vertical stand-off distance h^* and the groove width w^*. Among these, h^* exerts the dominant control on the spatio-temporal peak wall-shear stress by determining the jet morphology and the thickness of the liquid layer between the bubble's lower surface and the groove bottom.

The horizontal offset parameter d^* mainly governs the propagation direction and spatial distribution of the shear flow. Bubbles initiated closer to the channel centre ($d^* = 0$) produce more spatially uniform shear flow, whereas the influence of d^* on the maximum spatio-temporal shear stress is relatively minor, with variations of approximately 25 % relative to the peak value at $d^* = -0.5$ ($\approx$100 kPa).

The groove width w^* controls the extent of bubble trapping in both the x and z-directions and thereby modifies the microjet morphology. For moderate h^*, the maximum wall-shear stress first increases and then decreases with increasing w^*. As w^* becomes sufficiently large, the dynamics approaches that of an axisymmetric wall-proximal cavitation bubble near a flat surface, consistent with previous studies (Zeng *et al.* 2022).

The present simulations include surface tension and assume a hydrophilic wetted-wall condition, consistent with the experimental surface. Varying the surface tension does not substantially change the overall spatio-temporal pattern of the wall-shear stress, but it quantitatively modifies the jet velocity, daughter-bubble fragmentation and peak stress. In the cases considered here, an intermediate surface tension produces the largest jet velocity and hence the highest wall-shear stress. Dynamic wetting effects, contact-line motion and possible transitions between Cassie–Baxter and Wenzel states are not explicitly resolved in the present model. These effects may become important for surfaces with different wettability, hierarchical roughness or gas-entrapping textures and should be incorporated in future models of the cavitation dynamics near complex microstructured boundaries.

While the dynamics of a single wall-proximal cavitation bubble has been extensively studied, the present results reveal previously unresolved three-dimensional fluid-mechanical features associated with bubble collapse inside narrow, structured grooves. Future work should further examine the roles of wetting condition, bubble size and multi-bubble interactions, together with continued development of experimental techniques for resolving transient wall stress. Promising approaches include micro-pillar sensors, microscopic particle-tracking methods (Fuchs *et al.* 2023) combined with total-internal-reflection-fluorescence microscopy (Chan & Ohl 2012) and stress-sensitive coatings (Sun *et al.* 2022; Yokoyama *et al.* 2026). The configurations considered here provide a basis for understanding shear-flow generation over more complex surface topologies, including pillar-type microstructures (Kim & Kim 2014; Gonzalez-Parra *et al.* 2022), hierarchical textures (Gonzalez-Avila *et al.* 2020*a*; Devia-Cruz *et al.* 2024) and porous materials (Andrews *et al.* 2023), to name a few, thereby offering a pathway towards more realistic prediction of cavitation-induced surface loading in engineered systems.

Supplementary movies. Supplementary movies are available at https://doi.org/10.1017/jfm.2026.12123.

Acknowledgements. The anonymous referees are acknowledged for their very helpful suggestions to improve the manuscript.

Funding. This research was funded by the National Natural Science Foundation of China under grant nos. 12302313, 12402282 and 52525102.

Declaration of interests. The authors report no conflict of interest.

https://doi.org/10.1017/jfm.2026.12123 Published online by Cambridge University Press

References

Andrews, E.D., Fernández Rivas, D. & Peters, I.R. 2023 Bubble collapse near porous plates. *J. Fluid Mech.* **962**, A11.

Andrews, E., Rivas, D.F. & Peters, I.R. 2020 Cavity collapse near slot geometries. *J. Fluid Mech.* **901**, A29.

Beig, S.A., Aboulhasanzadeh, B. & Johnsen, E. 2018 Temperatures produced by inertially collapsing bubbles near rigid surfaces. *J. Fluid Mech.* **852**, 105–125.

Blake, J.R., Taib, B.M. & Doherty, G. 1986 Transient cavities near boundaries. Part 1. Rigid boundary. *J. Fluid Mech.* **170**, 479–497.

Brackbill, J.U., Kothe, D.B. & Zemach, C. 1992 A continuum method for modeling surface tension. *J. Comput. Phys.* **100** (2), 335–354.

Brujan, E.-A., Keen, G.S., Vogel, A. & Blake, J.R. 2002 The final stage of the collapse of a cavitation bubble close to a rigid boundary. *Phys. Fluids* **14** (1), 85–92.

Brujan, E.-A., Noda, T., Ishigami, A., Ogasawara, T. & Takahira, H. 2018 Dynamics of laser-induced cavitation bubbles near two perpendicular rigid walls. *J. Fluid Mech.* **841**, 28–49.

Brujan, E.A., Zhang, A.M., Liu, Y.L., Ogasawara, T. & Takahira, H. 2022 Jetting and migration of a laser-induced cavitation bubble in a rectangular channel. *J. Fluid Mech.* **948**, A6.

Cattaneo, M., Presse, L. & Supponen, O. 2025 Faraday wave singularities trigger microbubble jetting. *Phys. Rev. Lett.* **135** (20), 204002.

Cerbus, R.T., Chraibi, H., Tondusson, M., Petit, S., Soto, D., Devillard, R., Delville, J.P. & Kellay, H. 2022 Experimental and numerical study of laser-induced secondary jetting. *J. Fluid Mech.* **934**, A14.

Chahine, G.L., Kapahi, A., Choi, J.K. & Hsiao, C.T. 2016 Modeling of surface cleaning by cavitation bubble dynamics and collapse. *Ultrason. Sonochem.* **29**, 528–549.

Chan, C.U. & Ohl, C.-D. 2012 Total-internal-reflection-fluorescence microscopy for the study of nanobubble dynamics. *Phys. Rev. Lett.* **109** (17), 174501.

Chao-Tsung, H., Jayaprakash, A., Kapahi, A., Choi, J.-K. & Chahine, G. 2014 Modelling of material pitting from cavitation bubble collapse. *J. Fluid Mech.* **755**, 142–175.

Coussios, C.C. & Roy, R.A. 2008 Applications of acoustics and cavitation to noninvasive therapy and drug delivery. *Annu. Rev. Fluid Mech.* **40** (1), 395–420.

Devia-Cruz, L.F., Gonzalez-Parra, J.C., Cuando-Espitia, N., Robles, V., Aguilar, G. & Camacho-Lopez, S. 2024 Enhanced mitigation of cavitation erosion by means of femtosecond pulsed laser-induced hierarchical surface structures. *Surface Coat. Technol.* **481**, 130627.

Dijkink, R. & Ohl, C.-D. 2008 Measurement of cavitation induced wall shear stress. *Appl. Phys. Lett.* **93** (25), 254107.

Eleanor, S. & Constantin, C. 2019 Nucleation, mapping and control of cavitation for drug delivery. *Nat. Rev. Phys.* **1** (8), 495–509.

Fan, Y., Bussmann, A., Reuter, F., Bao, H., Adami, S., Gordillo, J.M., Adams, N. & Ohl, C.-D. 2024 Amplification of supersonic microjets by resonant inertial cavitation-bubble pair. *Phys. Rev. Lett.* **132** (10), 104004.

Fuchs, T., Bross, M. & Kähler, C.J. 2023 Wall-shear-stress measurements using volumetric μptv. *Exp. Fluids* **64** (6), 115.

Gonzalez-Avila, S.R., Nguyen, D.M., Arunachalam, S., Domingues, E.M., Mishra, H. & Ohl, C.-D. 2020*a* Mitigating cavitation erosion using biomimetic gas-entrapping microtextured surfaces (GEMS). *Sci. Adv.* **6** (13), eaax6192.

Gonzalez-Avila, S.R., Van, B., Charlotte, A., Zeng, Q. & Ohl, C.-D. 2020*b* Jetting and shear stress enhancement from cavitation bubbles collapsing in a narrow gap. *J. Fluid Mech.* **884**, A23.

Gonzalez-Parra, J.C., Robles, V., Devia-Cruz, L.F., Rodriguez-Beltran, R.I., Cuando-Espitia, N., Camacho-Lopez, S. & Aguilar, G. 2022 Mitigation of cavitation erosion using laser-induced periodic surface structures. *Surfaces Interfaces* **29**, 101692.

Greenshields, C.J. 2015 2015 Openfoam user guide. *OpenFOAM Found. Ltd. Vers.* **3** (1).

Hsiao, C.T., *et al.* 2013 Modelling single- and tandem-bubble dynamics between two parallel plates for biomedical applications. *J. Fluid Mech.* **716**, 137–170.

Jana, S.K. & Bhaskarwar, A.N. 2010 Modeling gas absorption accompanied by chemical reaction in bubble column and foam-bed slurry reactors. *Chem. Engng Sci.* **65** (11), 3649–3659.

Kim, T.-H. & Kim, H.-Y. 2014 Disruptive bubble behaviour leading to microstructure damage in an ultrasonic field. *J. Fluid Mech.* **750**, 355–371.

Kim, W., Kim, T.-H., Choi, J. & Kim, H.-Y. 2009 Mechanism of particle removal by megasonic waves. *Appl. Phys. Lett.* **94** (8), 081908.

https://doi.org/10.1017/jfm.2026.12123 Published online by Cambridge University Press

KOCH, M., LECHNER, C., REUTER, F., KÖHLER, K., METTIN, R. & LAUTERBORN, W. 2016 Numerical modeling of laser generated cavitation bubbles with the finite volume and volume of fluid method, using OpenFOAM. *Comput. Fluids* **126**, 71–90.

KUCHERENKO, V.V. & SHAMKO, V.V. 1986 Dynamics of electric-explosion cavities between two solid parallel walls. *J. Appl. Mech. Tech. Phys.* **27**, 112–115.

LANDEL, J.R. & WILSON, D.I. 2021 The fluid mechanics of cleaning and decontamination of surfaces. *Annu. Rev. Fluid Mech.* **53** (1), 147–171.

LIU, S., WANG, B., LI, S.-M., ZHANG, A.-M., PU, C. & ZENG, Q. 2026 Jet formation in air bubbles induced by cavitation bubbles. *J. Fluid Mech.* **1035**, A19.

MIFSUD, J., LOCKERBY, D.A., CHUNG, Y.M. & JONES, G. 2021 Numerical simulation of a confined cavitating gas bubble driven by ultrasound. *Phys. Fluids* **33** (12), 122114.

MILLER, S.T., JASAK, H., BOGER, D.A., PATERSON, E.G. & NEDUNGADI, A. 2013 A pressure-based, compressible, two-phase flow finite volume method for underwater explosions. *Comput. Fluids* **87**, 132–143. uSNCCM Moving Boundaries.

MOHAMMADZADEH, M., LI, F. & OHL, C.-D. 2017 Shearing flow from transient bubble oscillations in narrow gaps. *Phys. Rev. Fluids* **2** (1), 014301.

MOLEFE, L. & PETERS, I.R. 2019 Jet direction in bubble collapse within rectangular and triangular channels. *Phys. Rev. E* **100** (6-1), 063105.

NAGALINGAM, N., RAGHUNATHAN, A., KOREDE, V., POELMA, C., SMITH, C.S., HARTKAMP, R., PADDING, J.T. & ERAL, H.B. 2023 Laser-induced cavitation for controlling crystallization from solution. *Phys. Rev. Lett.* **131** (12), 124001.

OHL, C.-D., ARORA, M., IKINK, R., DE JONG, N., VERSLUIS, M., DELIUS, M. & LOHSE, D. 2006*a* Sonoporation from jetting cavitation bubbles. *Biophys. J.* **91** (11), 4285–4295.

OHL, C.-D., ARORA, M., RORY, D., JANVE, V.A. & LOHSE, D. 2006*b* Surface cleaning from laser-induced cavitation bubbles. *Appl. Phys. Lett.* **89** (7), 074102.

PHARES, D.J., SMEDLEY, G.T. & FLAGAN, R.C. 2000 The wall shear stress produced by the normal impingement of a jet on a flat surface. *J. Fluid Mech.* **418**, 351–375.

PHILIPP, A. & LAUTERBORN, W. 1998 Cavitation erosion by single laser-produced bubbles. *J. Fluid Mech.* **361**, 75–116.

POULAIN, S., GUENOUN, G., GART, S., CROWE, W. & JUNG, S. 2015 Particle motion induced by bubble cavitation. *Phys. Rev. Lett.* **114**, 214501.

RAU, K.R., QUINTO-SU, P.A., HELLMAN, A.N. & VENUGOPALAN, V. 2006 Pulsed laser microbeam-induced cell lysis: time-resolved imaging and analysis of hydrodynamic effects. *Biophys. J.* **91** (1), 317–329.

REESE, H., OHL, S.-W. & OHL, C.-D. 2023 Cavitation bubble induced wall shear stress on an elastic boundary. *Phys. Fluids* **35** (7), 076122.

REUTER, F., DEITER, C. & OHL, C.-D. 2022*a* Cavitation erosion by shockwave self-focusing of a single bubble. *Ultrason. Sonochem.* **90**, 106131.

REUTER, F. & KAISER, S.A. 2019 High-speed film-thickness measurements between a collapsing cavitation bubble and a solid surface with total internal reflection shadowmetry. *Phys. Fluids* **31** (9), 097108.

REUTER, F., LAUTERBORN, S., METTIN, R. & LAUTERBORN, W. 2017 Membrane cleaning with ultrasonically driven bubbles. *Ultrason. Sonochem.* **37**, 542–560.

REUTER, F. & METTIN, R. 2018 Electrochemical wall shear rate microscopy of collapsing bubbles. *Phys. Rev. Fluids* **3** (6), 063601.

REUTER, F., ZENG, Q. & OHL, C.-D. 2022*b* The rayleigh prolongation factor at small bubble to wall stand-off distances. *J. Fluid Mech.* **944**, A11.

ROBERTS, M.S. & JACOBS, J.W. 2016 The effects of forced small-wavelength, finite-bandwidth initial perturbations and miscibility on the turbulent Rayleigh–Taylor instability. *J. Fluid Mech.* **787**, 50–83.

RUSCHE, H. 2003 Computational fluid dynamics of dispersed two-phase flows at high phase fractions. PhD thesis, Imperial College London (University of London).

RUSCHE, H. 2015 *Computational Fluid Dynamics of Dispersed Two-Phase Flows at High Phase Fractions*. Imperial College, University of London.

SUN, T.-P., ÁLVAREZ-NOVOA, F., ANDRADE, K., GUTIÉRREZ, P., GORDILLO, L. & CHENG, X. 2022 Stress distribution and surface shock wave of drop impact. *Nat. Commun.* **13** (1), 1703.

TAGAWA, Y. & PETERS, I.R. 2018 Bubble collapse and jet formation in corner geometries. *Phys. Rev. Fluids* **3**, 081601.

TALEGHANI, M.H., KHODADADI, S., MADDAHIAN, R. & MOKHTARI-DIZAJI, M. 2023 Enhancing the bubble collapse energy using the electrohydrodynamic force. *Phys. Fluids* **35** (5), 053316.

https://doi.org/10.1017/jfm.2026.12123 Published online by Cambridge University Press

TRUMMLER, T., BRYNGELSON, S.H., SCHMIDMAYER, K., SCHMIDT, S.J., COLONIUS, T. & ADAMS, N.A. 2020 Near-surface dynamics of a gas bubble collapsing above a crevice. *J. Fluid Mech.* **899**, A16.

UBBINK, O. 1997 *Numerical Prediction of Two Fluid Systems with Sharp Interfaces*. Imperial College, University of London.

VERHAAGEN, B. & RIVAS, D.F. 2016 Measuring cavitation and its cleaning effect. *Ultrason. Sonochem.* **29**, 619–628.

VERON, F., HOPKINS, C., HARRISON, E.L. & MUELLER, J.A. 2012 Sea spray spume droplet production in high wind speeds. *Geophys. Res. Lett.* **39** (16), L16602.

WANG, Q., MAHMUD, M., CUI, J., SMITH, W.R. & WALMSLEY, A.D. 2020 Numerical investigation of bubble dynamics at a corner. *Phys. Fluids* **32** (5), 053306.

WU, S., ZUO, Z., STONE, H.A. & LIU, S. 2017 Motion of a free-settling spherical particle driven by a laser-induced bubble. *Phys. Rev. Lett.* **119** (8), 084501.

XIE, R.-Z., LI, S.-M., ZHANG, A.-M., XIE, D.-H., AN, H., TAN, B.H. & ZENG, Q. 2026 How slip length influences wall shear stress from jetting cavitation bubbles. *J. Fluid Mech.* **1040**, A31.

YOKOYAMA, Y., MARUOKA, H., MATSUNUMA, K. & TAGAWA, Y. 2026 Scaling crossover in droplet impact force on elastic substrates. *Nat. Commun.* **17** (1), 607.

ZENG, Q. 2020 Jetting from cavitation bubbles in viscous and confined liquids. PhD thesis, Nanyang Technological University.

ZENG, Q., AN, H. & OHL, C.-D. 2022 Wall shear stress from jetting cavitation bubbles: influence of the stand-off distance and liquid viscosity. *J. Fluid Mech.* **932**, A14.

ZENG, Q., GONZALEZ-AVILA, S.R., DIJKINK, R., KOUKOUVINIS, P., GAVAISES, M. & OHL, C.-D. 2018 Wall shear stress from jetting cavitation bubbles. *J. Fluid Mech.* **846**, 341–355.

ZENG, Q., GONZALEZ-AVILA, S.R. & OHL, C.-D. 2020 Splitting and jetting of cavitation bubbles in thin gaps. *J. Fluid Mech.* **896**, A28.

ZENG, Q.-Y., ZHANG, A.-M., TAN, B.-H., AN, H. & OHL, C.-D. 2024 Jetting enhancement from wall-proximal cavitation bubbles by a distant wall. *J. Fluid Mech.* **987**, R2.

ZHANG, A.-M., LI, S.-M., XU, R.-Z., PEI, S.-C., LI, S. & LIU, Y.-L. 2024 A theoretical model for compressible bubble dynamics considering phase transition and migration. *J. Fluid Mech.* **999**, A58.

ZHANG, S., DUNCAN, J.H. & CHAHINE, G. 2006 The final stage of the collapse of a cavitation bubble near a rigid wall. *J. Fluid Mech.* **257**, 147–181.

https://doi.org/10.1017/jfm.2026.12123 Published online by Cambridge University Press